

LITHIUM-DRIFTED DETECTORS

LITHIUM-DRIFTED  
GAMMA RADIATION DETECTORS

by

DAVID ALEXANDER MCKAY, B. Sc.

A Thesis

Submitted to the Faculty of Graduate Studies  
in Partial Fulfilment of the Requirements  
for the Degree  
Master of Science

McMaster University

September, 1964

MASTER OF SCIENCE (1964)  
(Physics)

McMASTER UNIVERSITY  
Hamilton, Ontario.

TITLE: Lithium-Drifted Gamma Radiation Detectors

AUTHOR: David Alexander McKay, B. Sc. (University of  
British Columbia)

SUPERVISOR: Dr. G. L. Keech

NUMBER OF PAGES: vii, 64

SCOPE AND CONTENTS:

An investigation has been made of the theory, fabrication and performance of lithium-drifted p-i-n junction detectors. A method is described for the preparation of counters with sufficiently deep depletion layers for the detection of a wide range of gamma energies. Four-point probe resistivity measurements are used to carry out a detailed investigation of the preliminary lithium diffusion, and several discrepancies with theoretical predictions are discussed. The resolution of a Compton spectrometer system using this type of detector is examined and compared with some calculated values.

## ACKNOWLEDGEMENTS

The author wishes to express his appreciation to his Research Director, Dr. G. L. Keech, for the guidance and assistance which he has provided throughout this research. He would also like to thank Dr. W. V. Prestwich and Mr. L. B. Hughes for numerous discussions and suggestions, particularly concerning the detector fabrication process, and Mr. I. B. Webster for the preparation of many of the final drawings.

## TABLE OF CONTENTS

	Page
CHAPTER I INTRODUCTION	1
CHAPTER II THEORY	3
2.1 Principle of Operation	3
2.2 The p-n Junction	5
2.3 The Diffusion Process	8
2.4 The Ion-Drift Process	9
2.5 Noise and Energy Resolution	12
(a) Statistical Fluctuations	12
(b) Current Noise	13
CHAPTER III DETECTOR FABRICATION	15
3.1 Preparation of the Silicon	15
3.2 The Lithium Diffusion-p-n Junction	16
3.3 The Ion-Drift	19
CHAPTER IV FOUR-POINT PROBE MEASUREMENTS	23
4.1 Theory	23
(a) Measurement of Resistivity	23
(b) Measurement of Sheet Resistivity	28
4.2 Experimental	29
(a) Apparatus	29
(b) Reliability Determinations	31
(c) Measurement of Alloy Depth and Uniformity	33
(d) Measurement of Intrinsic Region after Drifting	42
CHAPTER V DETECTOR RESPONSE	47
5.1 Mounting the Detector	47
5.2 Experimental Results	47
(a) Singles Spectra	49
(b) Compton Spectrometer	51
(c) Spectrum of Cs <sup>134</sup>	60
REFERENCES	63

## LIST OF TABLES

Number	Title	Page
I	Compton Spectrometer Response and Window Width	59
II	Compton Spectrometer Response and NaI Crystal Position	59

## LIST OF ILLUSTRATIONS

Figure Number	Title	Page
1.	Band Scheme for a p-n Junction	7
2.	Illustration of the Ion-Drift Technique	10
3.	Alloying Oven	17
4.	Diode Characteristic	20
5.	Drift Apparatus	21
6.	The Four-Point Probe Method of Resistivity Measurement	24
7.	Correction Factors for Probes Perpendicular and Parallel to a Nonconducting Boundary	27
8.	The Four-Point Probe Apparatus	30
9.	Silicon Resistivity from Eq. 4.5	32
10.	Silicon Resistivity from Eq. 4.6	32
11.	Surface Resistivity of Alloyed Surface	34
12.	Theoretical Alloy Depth	34
13.	Depth Contour of Alloyed Surface	36
14.	Conductivity Profile of Lithium Diffused Region	38
15.	Lithium Concentration Profile	40
16.	Resistivity Profile of Drifted Diode	43
17.	Sectioned and Stained Diode after Drifting	45
18.	Detector Chamber Cross Section	48

Figure Number	Title	Page
19.	Cs <sup>137</sup> Spectrum	50
20.	Compton Spectrometer System	52
21.	Compton Spectrometer Response	54
22.	Compton Spectrometer Resolution	57
23.	Cs <sup>134</sup> Compton Spectrum	61

## CHAPTER I

### INTRODUCTION

In recent years, considerable advances in charged particle spectroscopy have been made through the use of solid state radiation detectors. The principle of operation of these counters is somewhat similar to that of a gas ionization chamber. In the latter, the incoming charged particle ionizes the gas and the electrons and positive ions so produced are collected at the electrodes by means of an applied field. In the case of the solid state counter, the incoming particle dislocates electrons from the lattice and the charge is carried by the electron-hole pairs rather than electron-ion pairs.

Since a much lower energy is required to produce an electron-hole pair, it follows that more pairs will be produced, so that a larger current pulse is created in the semiconductor for a given energy loss. Thus the statistical fluctuations will be smaller, and the resolution improved over that of the gas counter. In addition, the use of a solid as a detector means that a high stopping power may be achieved with only a thin sensitive layer. The small size of the solid state counter is a property which distinguishes it from most conventional counters.

The development of solid state radiation counters

began soon after the invention of the transistor in 1948. One of the earliest applications was that of McKay (1,2), who in 1949 used a p-n junction in germanium for the detection of alpha particles. By 1959, an extensive investigation was being made into the formation of junctions in silicon. Two types of junction detectors were produced, the surface barrier (3) and the diffused junction (4).

Neither of these types, however, had a sufficiently thick sensitive layer for the detection of gamma rays of more than several hundred keV. It was not until the development by Pell (5) of the ion-drift technique that detectors with sensitive regions of up to 4 mm. were developed (6-8). An improvement of this drift process by Miller et al. (9) has enabled sensitive regions of up to 1 cm., which gives sufficient stopping power to detect gamma rays of up to 6 MeV., to be produced. It is with the fabrication and properties of this last type of detector that this thesis is concerned.

## CHAPTER II

### THEORY

#### 2.1 Principle of Operation

Before examining the various mathematical details of the operation of a lithium-drifted gamma counter, a qualitative discussion of the process by which an incoming gamma ray is transformed into a current pulse is in order.

Through a photoelectric or a Compton interaction, or as the end result of a pair-production process, all or part of the gamma ray energy is transferred to one or more electrons. These electrons then move through the sensitive or depletion layer of the counter and lose their energy in the production of low-energy electrons by impact ionization. These collisions may lift an electron from the valence or other low-lying occupied bands to the conduction or other higher unoccupied bands, leaving behind it a vacancy or hole which may be considered as a carrier. Through a series of interactions, the electrons fall to the lowest available conduction band levels and the holes rise to the highest available valence band levels, a process requiring about  $10^{-12}$  sec.

If a potential is now applied across the terminals of the counter, the resultant field will sweep the electrons and holes across to the positive and negative terminals

occurs exponentially with a time constant  $T_0$ , the  
 in addition a reversion to electrical neutrality which  
 centers and thus a short recombination time.) There is  
 imperfections, then there will be many recombination  
 of the quality of the material used. (If there are many  
 called the recombination time  $T_r$ , and is a characteristic  
 collection. The characteristic time for this process is  
 valence band, so that it is no longer available for  
 effect returns an electron from the conduction to the  
 imperfection within the crystal. This recombination in  
 recombination center, which is essentially a structural  
 is possible for a hole and an electron to be captured by a  
 which is available for the collection of the charge. It  
 There is, however, a limit on the amount of time  
 with experiment.)  
 one hole-electron pair, a result which is in good agreement  
 vibrations of the solid, 3.5 eV. is necessary to produce  
 due to a strong coupling of the electrons to the lattice  
 silicon is 1.1 eV., Shockley (10) has calculated that  
 difference between the valence and conduction bands of  
 produce one hole-electron pair. (Although the energy  
 the particle energy divided by the energy required to  
 The number of pairs created by the particle is given by  
 proportional to the number of hole-electron pairs collected.  
 respectively. The current pulse produced is directly

dielectric relaxation time constant.

For efficient charge collection, it is clearly necessary that the carrier transit time  $\tau_t$ , that is the time required for a carrier to travel the entire width of the counter, be less than either  $\tau_r$  or  $\tau_o$ , which may be as low as  $10^{-6}$  sec. As  $\tau_t$  varies inversely as the applied field, it follows that a high field is required across the counter. This may not be achieved simply by the application of a high voltage as even for the purest silicon commercially available the resulting leakage current is sufficiently large that the random fluctuations in it could obscure the pulses arising from the collection of hole-electron pairs.

## 2.2 The p-n Junction.

One method of achieving a high field without the application of a high voltage is a reverse-biased p-n junction. In this work the junction is produced by diffusing lithium into p-type silicon which has been produced by doping with boron during crystal growth. The junction occurs at the point in the crystal where the two impurity concentrations are the same. The region on one side of this junction will be positively charged due to the excess of holes associated with the boron acceptor ions, while the region on the other side will be negatively charged on account of the excess of electrons associated with the lithium donor ions. This type of charge distrib-

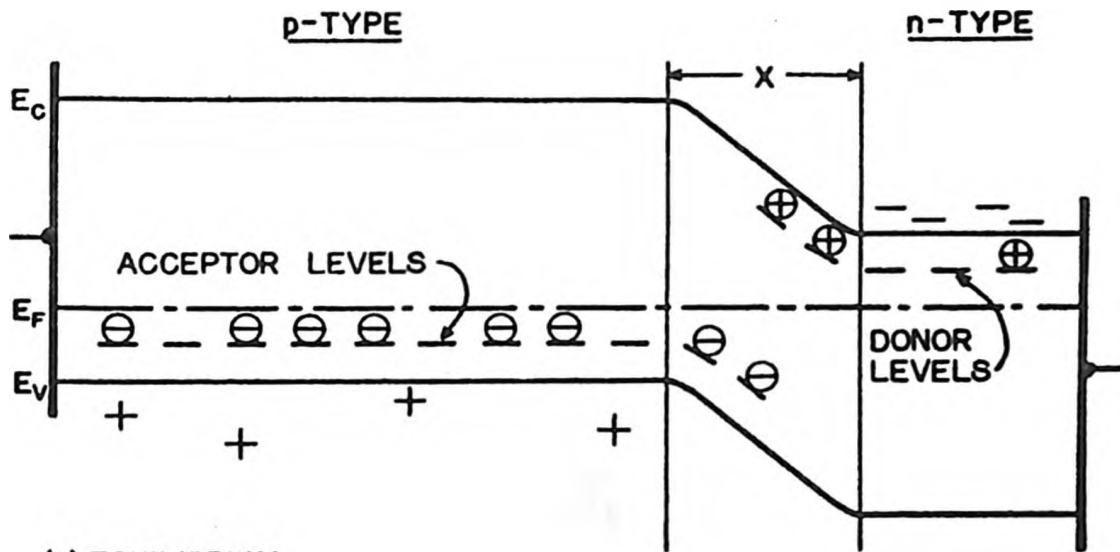
ution may be shown to create a potential barrier across the junction interface. The barrier is in fact a rectifying junction so that a diode results. This is shown in Figure 1 (a). The level  $E_c$  indicates the lower edge of the conduction band, while  $E_v$  represents the upper edge of the valence band. The Fermi level,  $E_f$ , lies close to the valence band in the p-type region because of the acceptor levels created by the boron impurity, while in the n-type region it is nearest the conduction band on account of the donor levels created by the lithium.

There is some movement of holes and electrons across this barrier so that a space charge region or depletion layer is created in which all donor and acceptor levels are completely filled. It is across this region that the potential difference and hence the high field exists, and this condition defines the sensitive region of the counter.

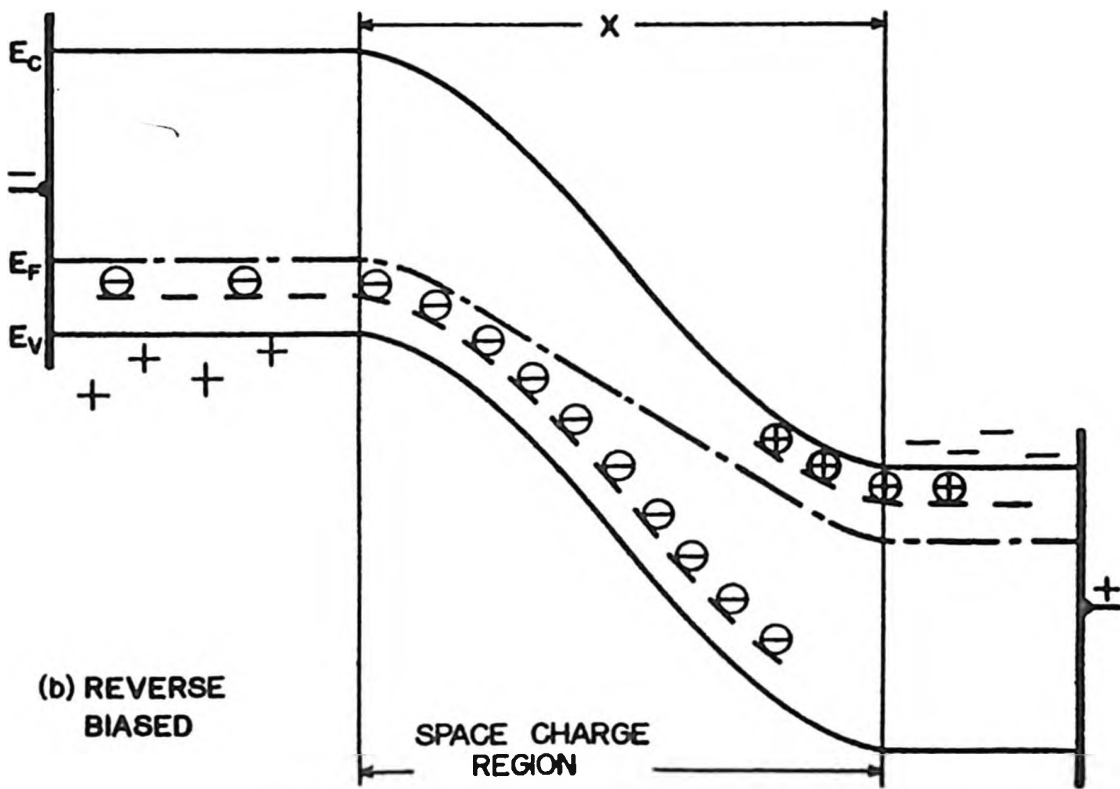
With no reverse bias applied, the potential difference is only .6 V. and extends over .01 mm. (11) If, however, the silicon crystal is reverse-biased, (that is a negative terminal connected to the p-type region and a positive terminal to the n-type region), both the barrier height and depletion layer depth are increased, as shown in Figure 1 (b). It has been shown (12) that for p-type silicon the depletion layer depth  $w$  is given by

$$w = 3.2 \times 10^{-5} (\rho V)^{\frac{1}{2}} \text{ cm.} \quad (2.1)$$

FIGURE 1



(a) EQUILIBRIUM



(b) REVERSE BIASED

BAND SCHEME FOR A p-n JUNCTION

where  $\rho$  is the resistivity in ohm-cm., and  $V$  is the applied voltage in volts. With an applied voltage of 300 Volts, and a resistivity of  $10^4$  ohm-cm., a depletion layer of about .5 mm. is obtained, so that the field is some 6000 Volts/cm., which ensures efficient charge collection.

While a sensitive region of .5 mm. is satisfactory for the detection of alpha particles and low energy electrons, it is not sufficient to stop electrons of several MeV. Hence some method is required which will considerably increase the depth of the depletion layer, in order to detect these particles. The ion-drift technique is such a method. Lithium is initially deposited on the surface of the silicon and then thermally diffused into it to form a p-n junction near the surface. A reverse bias is then applied to this junction to bring about the ion-drift.

### 2.3 The Diffusion Process

A mathematical treatment of the lithium diffusion is based on the familiar diffusion equation

$$\frac{\partial N}{\partial t} = D \frac{\partial^2 N}{\partial X^2} \quad (2.2)$$

where  $N$  is the concentration of the diffusing material, and  $D$  is the diffusion coefficient.

The exact solution to this equation depends on the

initial and boundary conditions which are chosen. Those generally used (5,8) are that the diffusion takes place from a constant source, that is the diffusant concentration at the surface is a constant  $N_0$  at all times. This is a reasonable assumption if a sufficiently large amount of lithium is initially deposited on the surface of the silicon crystal. In this case the solution to eq. 2.2 is (13)

$$\begin{aligned} N(x,t) &= N_0 \left( 1 - \operatorname{erf} \left( \frac{x}{2\sqrt{Dt}} \right) \right) \\ &= N_0 \operatorname{erfc} \left( \frac{x}{2\sqrt{Dt}} \right) \end{aligned} \quad (2.3)$$

where  $\operatorname{erfc}$  is the complementary error function defined by  $\operatorname{erfc} = 1 - \operatorname{erf}$ .

#### 2.4 The Ion-Drift Process

The distribution of the lithium after the initial diffusion is shown in Figure 2 (a). We have seen that if a reverse bias is applied to a p-n junction, an electrostatic field will be present in the depletion region around the original junction location. If the silicon diode is heated to a sufficient temperature to give the positive lithium ions an appreciable mobility, the force exerted by this field will cause a considerable movement of these ions from the lithium-rich side of the junction to the lithium-deficient side. There will also be a further thermal diffusion of the lithium, but because the diffusion constant is so much less than the drift velocity, it may be neglected.

FIGURE 2

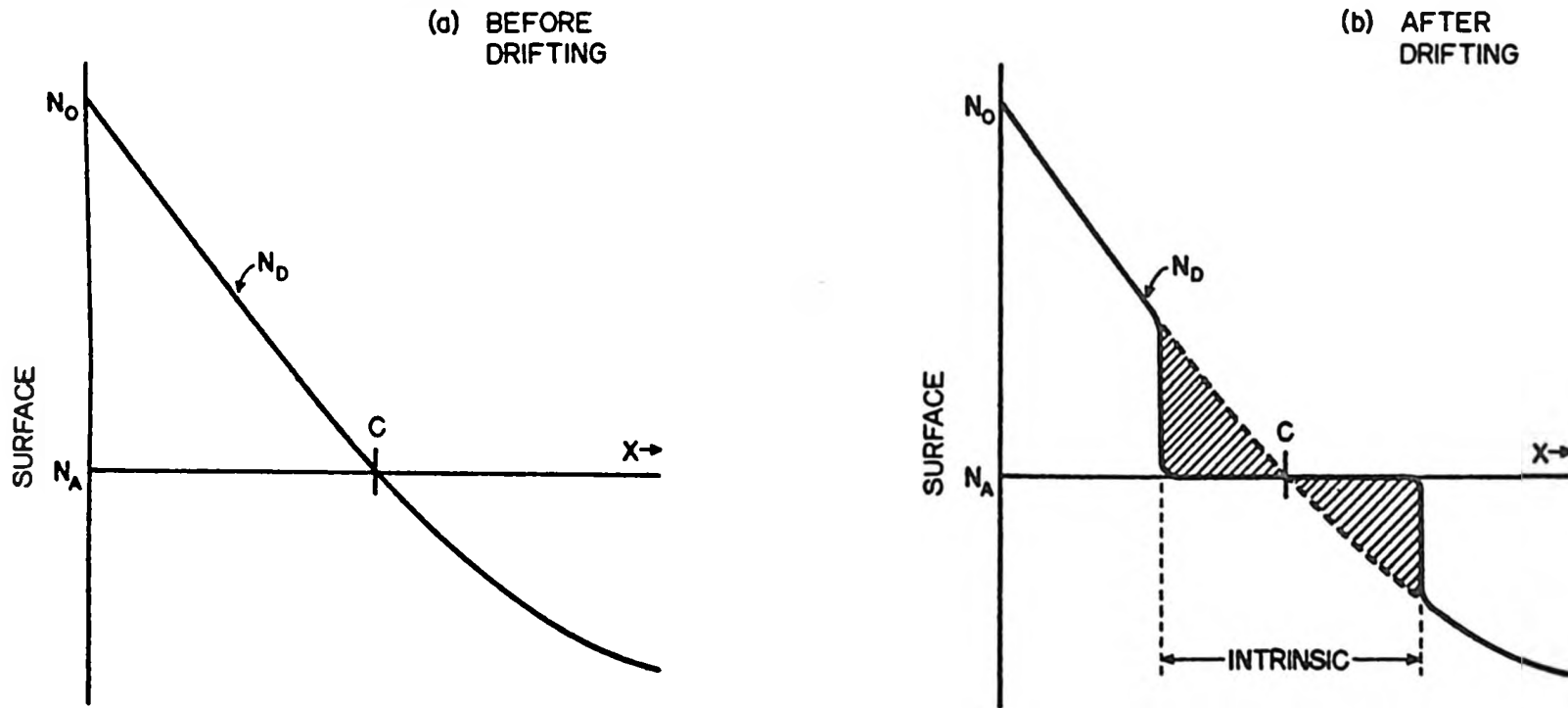


ILLUSTRATION OF THE ION-DRIFT TECHNIQUE

If  $x$  indicates the distance from the surface of the silicon crystal and  $x=c$  the original junction depth, then there will be a decrease in the lithium concentration in the region for which  $x < c$ , and a corresponding increase for  $x > c$ . It is not possible, however, for the lithium concentration to fall below the boron concentration in the region  $x < c$ , as this would result in a reversal of the charge concentration in this region and hence a reversal of the field, so that lithium ions would move into this region rather than out of it. Similarly it is not possible for the lithium concentration to rise above that of the boron in the region  $x > c$ .

The net result is that the lithium concentration decreases to the boron level at  $x < c$  and increases to it at  $x > c$ , so that a considerable intrinsic region is created in which the lithium and boron ions are entirely paired off and there are no donor or acceptor impurity levels. This region will then have a high resistivity and will be the high field area of the counter in which the charge is collected. This is shown in Figure 2(b). The two hatched regions indicate the amount of charge which has been drifted across the junction.

The rate of increase of the depth  $w$  of the intrinsic region is given by (9)

$$\frac{dw}{dt} = \mu \left( \frac{V}{w} \right) \quad (2.4)$$

where  $\mu$  is the lithium ion mobility in cm /volt-sec. and  $V$  the applied voltage. Multiplying both sides by the leakage current  $I$  gives

$$Iwdw = \mu IVdt \quad (2.5)$$

If the drift temperature is kept constant, so  $\mu$  is invariant and if  $I$  is proportional to  $w$  then both sides of eq. 2.5 may be integrated to give

$$K \int_0^w w^2 dw = \mu \int_0^T IVdt \quad (2.6)$$

where  $T$  is the total drift time and  $w$  the final intrinsic region width, from which

$$w = (K\mu J)^{1/3} \quad (2.7)$$

where  $K$  is a constant and  $J$  the total energy dissipated in the drift process. For deep drifts it has been found that the leakage current increases more slowly than  $w$ , and ultimately the cube root of eq. 2.7 becomes a square root (9).

## 2.5 Noise and Energy Resolution

There are two main factors which contribute to the resolution of any semiconductor junction detector, referred to as statistical fluctuations and noise.

### (a) Statistical Fluctuations

If the energy of the incoming particle is  $E$ , then the number of hole-electron pairs produced if it is completely stopped in the depletion layer is

$$n = \frac{E}{\epsilon} \quad (2.8)$$

where  $\mathcal{E}$  has been shown to be 3.6 eV. for silicon. If the Fano Factor is considered to be unity, (that is, the creation of each hole-electron pair is an independent event), then the standard deviation in  $n$  is given by  $\sqrt{n}$ . The standard deviation in the detector response due to statistics is then

$$\sigma = \mathcal{E} \sqrt{n} = \sqrt{\mathcal{E} E} \text{ eV.} \quad (2.9)$$

(b) Current Noise

Shockley (14) has shown that the reverse saturation current across a p-n diode junction is given by

$$I_s = e \left[ p_n \sqrt{\frac{D_p}{\tau_p}} + n_p \sqrt{\frac{D_n}{\tau_n}} \right] \quad (2.10)$$

where  $e$  is the electronic charge,  $p_n$  and  $n_p$  are the densities of holes in the n-type region and of electrons in the p-type region, respectively,  $D_p$ ,  $D_n$ ,  $\tau_p$  and  $\tau_n$  are the diffusion constants and lifetimes, respectively of holes and electrons in the regions where they are minority charges. This reverse current interrupts the movement of carriers and destroys the continuity of the current pulse arriving at the electrodes and thus creates noise within the counter.

From eq. 2.10 it may be seen that the reverse current is largest where the carrier lifetimes are the shortest. This will be in the region near the surface of the counter, where there is a greater density of recombination centres owing to structural damage incurred during the

fabrication. Thus surface leakage current is the main source of internal noise in the junction counter.

The external noise inherent in the amplification system must also be considered. The low-noise preamplifier and amplifier used in this work were found to have a noise resolution of 5 keV. as an isolated system.

It is of interest to note that only the resolution brought about by statistical fluctuations is dependent upon the energy of the incoming particle. As this is not a large contributor to the overall resolution, the latter is not strongly dependent energy. thus the percentage resolution will be much lower for high energy gamma rays than for those of low energy. This effect is in marked contrast to the sodium iodide scintillation counter, whose percentage resolution above 1 Mev. is virtually constant with energy.

CHAPTER III  
DETECTOR FABRICATION

3.1 Preparation of the Silicon

The specifications of the silicon used in the fabrication of these detectors were as follows:

a) p-type, with boron as impurity, b) resistivity 270 ohm-cm., c) Cylindrical bar 2 cm. in diameter, d) Single crystal, a  $\langle 111 \rangle$  direction parallel to the cylinder axis, e) carrier lifetime of 100 microseconds. A diamond saw was used to cut a one cm. deep slice from one of these bars. The saw was a Felker di-met model 80-BQ cutoff machine fitted with a bonded diamond wheel blade. The diamonds were 150 micron diameter and the total width of cut was .03 in. The rate of descent of the blade was governed by hydraulic pressure.

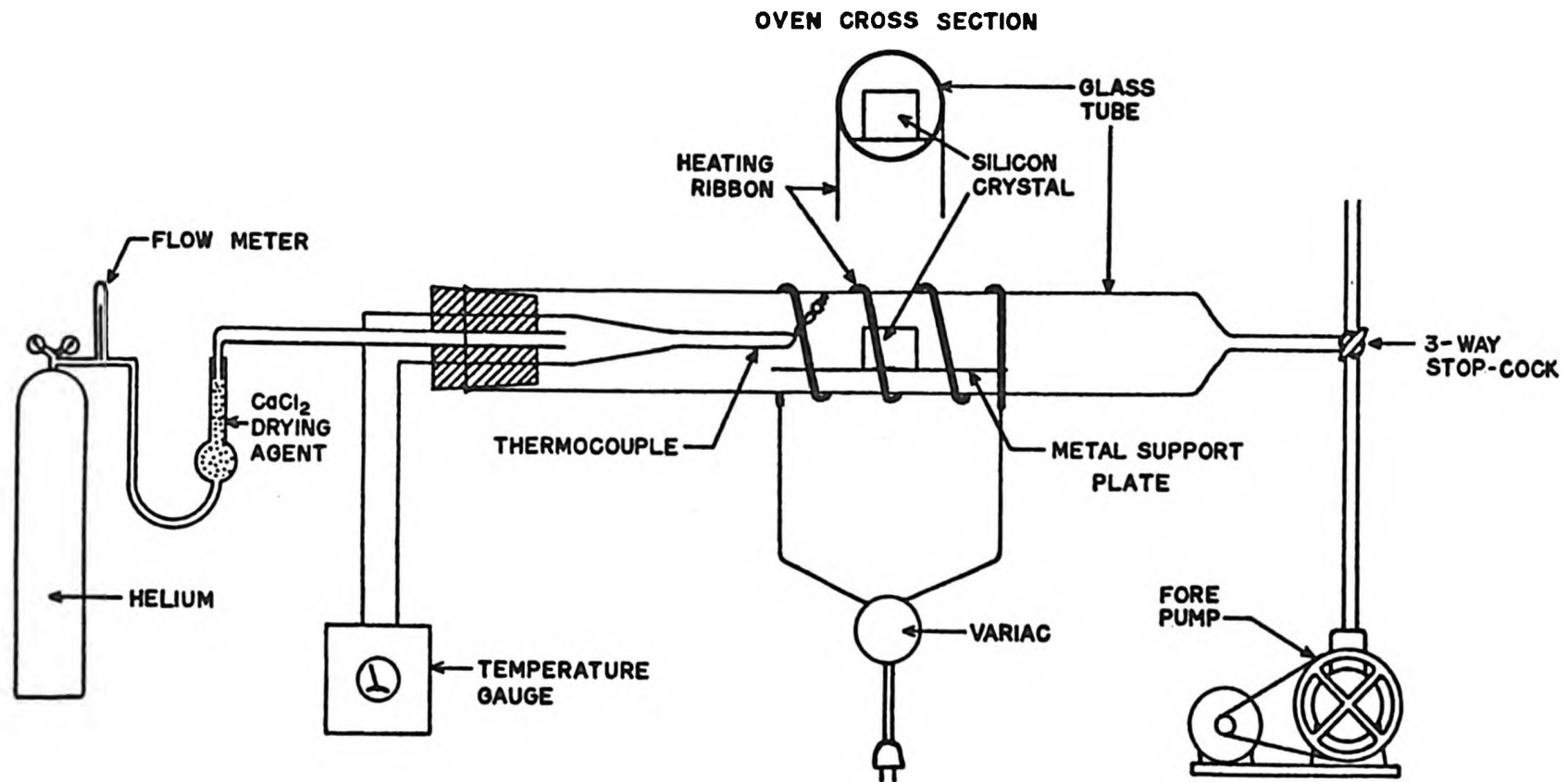
The slice was polished using silicon carbide of 220, 320, 400 and 600 grit to remove damage caused by the saw cut. After a lapping with 25 micron aluminum oxide, the silicon slice was washed thoroughly in a detergent, rinsed in demineralized water and allowed to dry. After this, care was taken to avoid any contamination of the slice.

### 3.2 The Lithium Diffusion

A thin layer of lithium in the form of a suspension in mineral oil was painted onto one face of the slice. This suspension was composed of 30% lithium, 69% mineral oil and 1% oleic acid and was obtained from the Lithium Corporation of America. The slice was then placed in the alloying oven shown in Figure 3 to carry out the diffusion process. The silicon slice and support plate were placed as level as possible in the oven. Following this step the system was evacuated and purged with helium to remove all oxygen from the oven. As a further precaution, a low helium flow was maintained throughout the process to ensure that no oxygen reached the lithium before the alloying was completed, as the violence of the resulting oxidation was found to cause considerable pitting of the silicon slice.

The temperature of the oven was raised to 225°C. by passing a current through a heater formed by several layers of nichrome wire wrapped about the central section of the oven. A variac was used to control the current flow and hence the rate of heating. The temperature was monitored by means of a thermocouple which was placed in contact with the oven wall since direct thermal contact to the slice itself was not feasible. The temperature was held at 225°C. for 20 min. to burn off the mineral oil and free the lithium for alloying into the silicon.

FIGURE 3



ALLOYING OVEN

The diffusion was brought about by rapidly raising the temperature to  $400^{\circ}\text{C}$ ., where it was held for five to ten minutes. Following this the slice was cooled slowly to room temperature and washed in methanol to remove the lithium residue.

It was then nickel plated by an electroless method developed by Sullivan and Eigler (15). This enabled electrical contact to be made to the diode. The faces of the slice were protected with a layer of opiazon wax and the nickel removed from the edge using an etch consisting of two parts nitric acid, two parts acetic acid and one part hydrofluoric acid.

Measurement of the back-resistance of the slice at this stage yielded a rather low value, indicating that a poor rectifying junction had been formed. Observations of the slice made during the initial heating indicated that there had been a slight withdrawal by the lithium oil suspension from the edge of the slice. (This was confirmed by the four-point probe measurements described in Chapter IV). This would result in little or no lithium near the edge, and hence a poor rectifying junction.

The situation was remedied by grinding about .5 mm. off the outer edge of the slice to remove the lithium-deficient region. After grinding, the slice was etched again to remove surface damage and cleaned thoroughly in methanol and trichloroethylene. The back resistance was

again measured and found to be much improved. (After this discovery was made, the initial etch was eliminated from the procedure and the nickel taken off the edge during the grinding.) The diode characteristic was measured and the result, shown in Figure 4, indicates that a good rectifying junction has been formed and that the drift process may now be commenced.

#### 4.2 The Ion-Drift

The apparatus used during the ion-drift process is shown in Figure 5. The phosphor-bronze spring performs the dual function of providing electrical contact to the diode and holding it in place. The fluorocarbon liquid, in this case FC43, also performs several functions. First, it is used as a contact medium for the preliminary heating of the diode to a temperature at which an appreciable drift power may be applied to it. Second, it serves as a vapour phase coolant to maintain the diode at a constant temperature at which the drift voltage does not result in diode breakdown. (Although the lithium ion mobility increases exponentially with temperature, the drift rate is essentially independent of temperature because there is a similar increase in the leakage current). Finally it keeps the junction edges clean, thus minimizing this leakage current.

The drift power was obtained from a constant wattage power supply patterned on one developed by Miller et al. (9). A constant power output is necessary to prevent

FIGURE 4

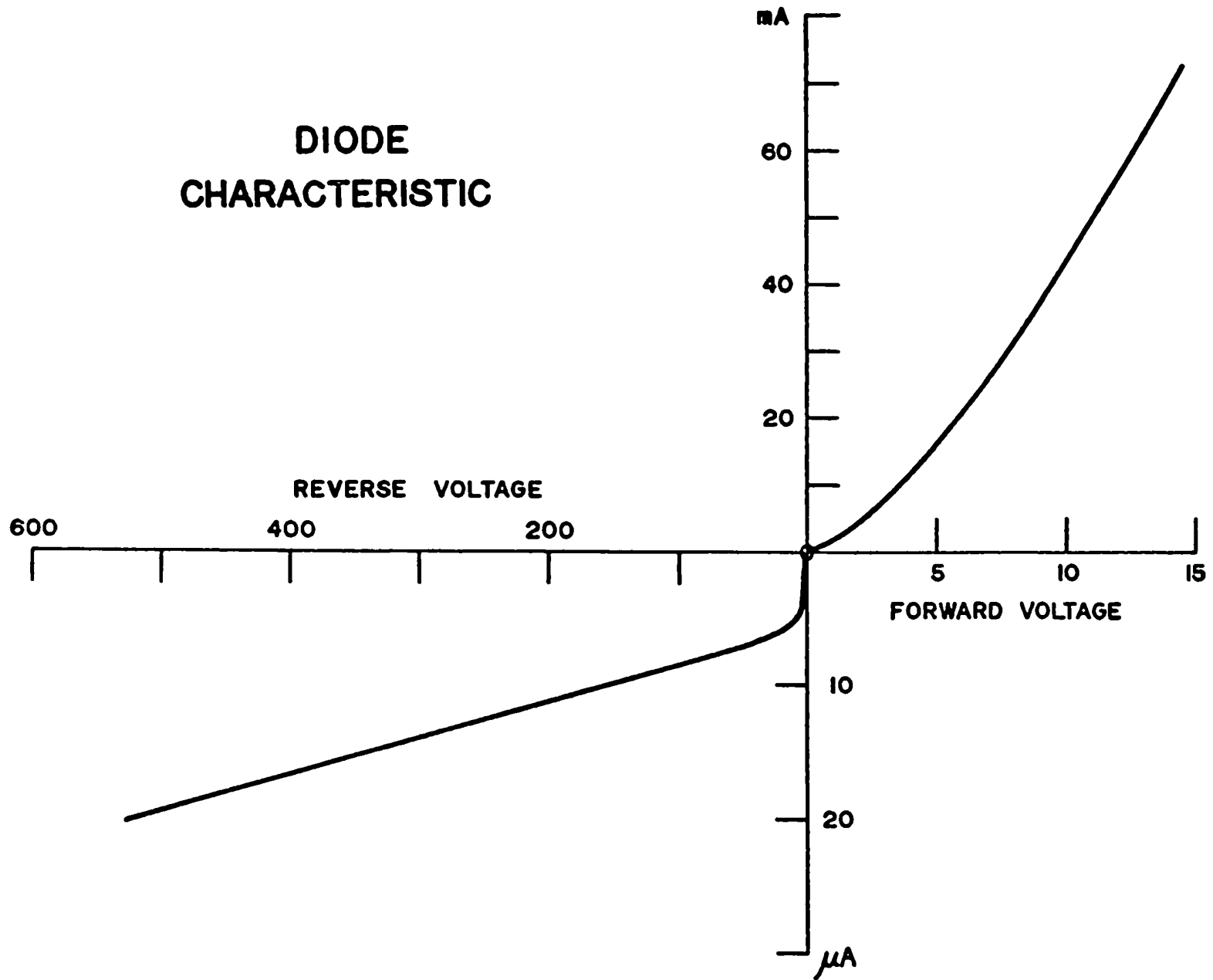
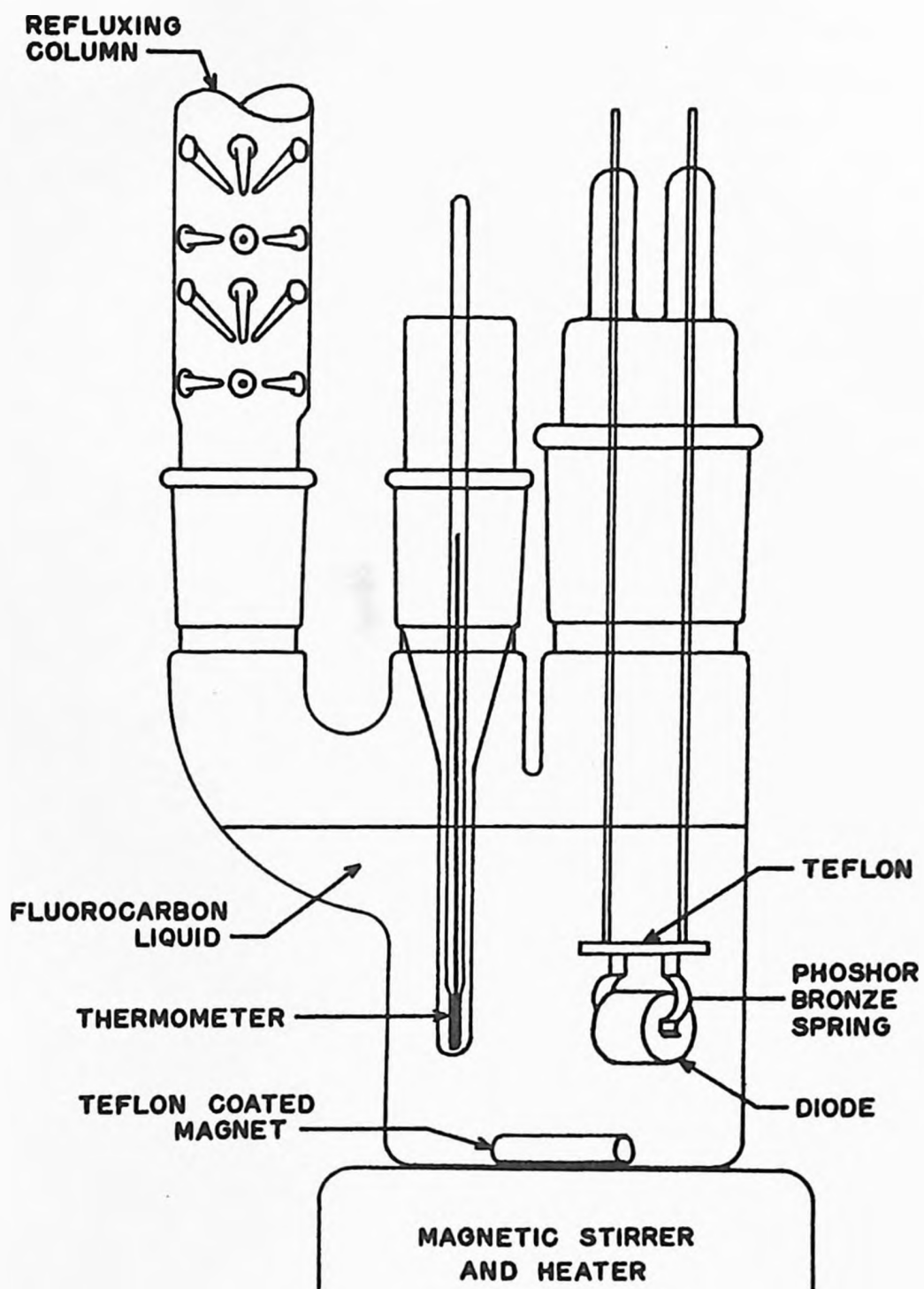


FIGURE 5



DRIFT APPARATUS

a temperature-current feedback system from developing and causing a breakdown of the diode. An increase in temperature causes more current to be drawn through the diode which in turn causes more heating, and so on. The power supply provided a sawtooth form voltage of 300 V. magnitude, which was produced essentially by the discharge of a capacitor across the diode. The amount of power provided was varied by adjusting the current output.

At the start of the drift, an external heater was used to bring the fluorocarbon to equilibrium at about  $160^{\circ}\text{C}$ , at which time the power supply was connected so as to back-bias the diode. In general a drift power of between 20 and 60 watts was used. Once this power was applied to the diode, little heat was required from the external heater, as electrical heating within the diode itself was almost sufficient to maintain the fluorocarbon at equilibrium.

A typical example of the drifting power and times used is a power of 50 w. applied for a period of about 7 days. Measurements described in Chapter IV showed that this was sufficient to produce a depletion layer some 8 or 9 mm. thick.

CHAPTER IV  
FOUR-PO. VT PROBE MEASUREMENTS

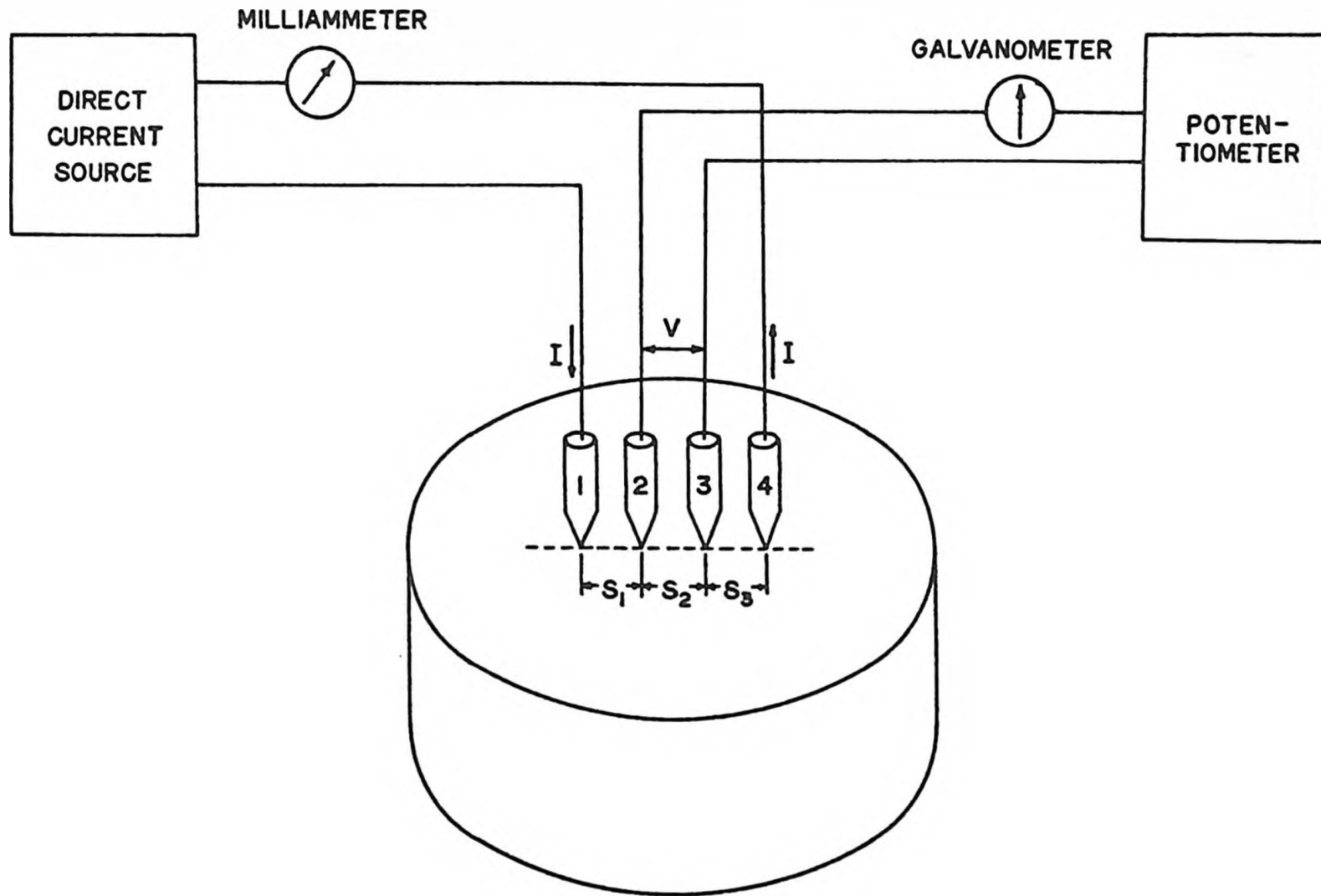
4.1 Theory

(a) Measurement of Resistivity

The usual methods used to measure resistivity are not applicable to semiconductors since these methods require that the potential be measured across the same electrodes that are used to pass the current. This is feasible only if the contact resistance between the samples and the electrode is negligible; whereas contacts between a metal electrode and a semiconductor sample are generally rectifying. There is in addition the problem of minority carrier injection at the electrodes, which affects the measured resistivity of the sample.

The four-point probe method, developed by Valdes (16), uses ohmic contacts to minimize this minority carrier injection. As shown in Figure 6, four sharply pointed collinear probes are lowered onto the surface of the sample, which is usually lapped, both to minimize any slipping of the probes, and to provide a high combination rate for minority carrier elimination. The current is passed through

FIGURE 6



THE FOUR-POINT PROBE METHOD OF RESISTIVITY MEASUREMENT

probes 1 and 4, and the floating potential between probes 2 and 3 is measured.

It may be shown from a solution of LaPlace's equation (17) that the floating potential induced at a point by an electrode carrying a current  $I$  is given by

$$V_f = \frac{\rho I}{2\pi r} \quad (4.1)$$

where  $r$  is the distance of the point from the electrode, and  $\rho$  is the resistivity of the material. In the case of the four-point probe, probes 1 and 4 are electrodes carrying currents of opposite sign, so that the potentials they induce at probes 2 and 3 will also be opposite. Thus from eq. 4.1

$$V_{f2} = \frac{\rho I}{2\pi} \left( \frac{1}{s_1} - \frac{1}{s_2+s_3} \right) \quad (4.2)$$

$$V_{f3} = \frac{\rho I}{2\pi} \left( \frac{1}{s_1+s_2} - \frac{1}{s_3} \right) \quad (4.3)$$

where  $s_1$ ,  $s_2$ , and  $s_3$  are the probe spacings as shown in the figure.

Since the potential measured is just  $V = V_{f2} - V_{f3}$ , the resistivity may be computed as

$$\rho = \frac{V}{I} \frac{2\pi}{\left\{ \frac{1}{s_1} + \frac{1}{s_2} - \frac{1}{s_1+s_2} - \frac{1}{s_2+s_3} \right\}} \quad (4.4)$$

If we have equal probe spacing, so that  $s_1=s_2=s_3=s$ , this simplifies to

$$\rho = \frac{V}{I} 2\pi s \quad (4.5)$$

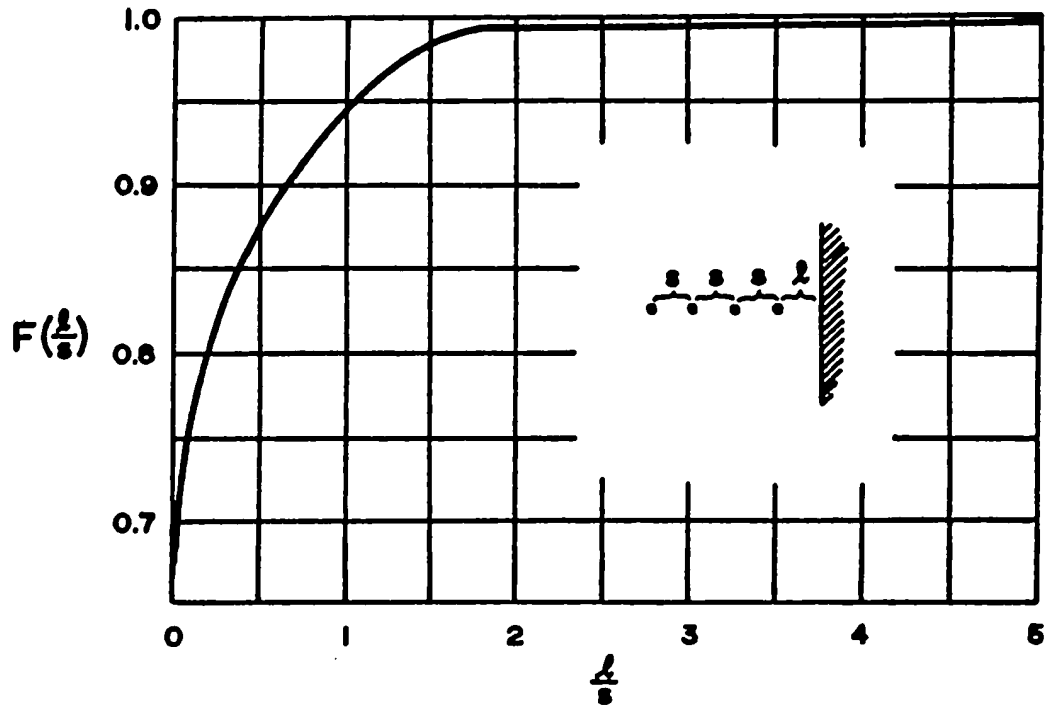
Generally,  $V$  is in volts,  $I$  in amps.,  $s$  in cms., and  $\rho$  in ohm-cm.

Eq. 4.5 applies, however, only if the probes are placed sufficiently far from all other surfaces of the sample so that they may be considered to rest on a semi-infinite volume. If they are near one of the other surfaces, then images of the two current sources are produced on the other side of this boundary. These images are opposite in sign to their respective sources if the boundary is conducting and similar in sign if it is non-conducting. These images will also produce floating potentials at the inner probes, and these must be considered when calculating the resistivity. This effect is taken into account by modifying eq. 4.5 to read

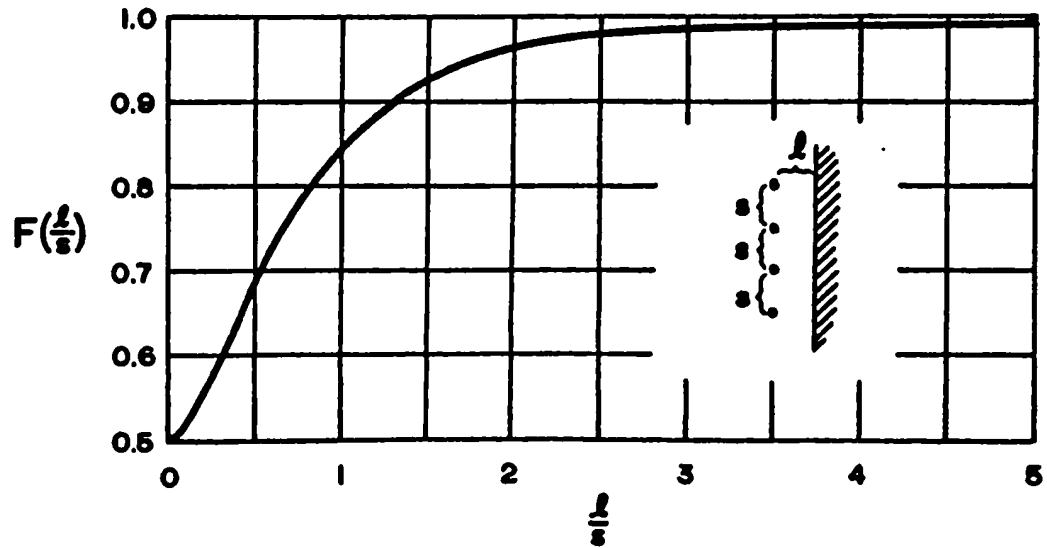
$$\rho = \frac{V}{I} 2\pi s F\left(\frac{l}{s}\right) \quad (4.6)$$

where  $l$  is a measure of the distance between the probes and the boundary. The form of  $F$  depends upon the type of boundary and the position of the probes relative to it. Graphs for two cases used as approximations to those encountered in this work, probes parallel and perpendicular to a non-conducting boundary, are shown in Figure 7. Since we have images of a similar sign to those they mirror, the floating voltages induced at the inner probes will be increased, thus  $F$  is always less than one. The opposite is

FIGURE 7



CORRECTION FACTOR FOR PROBES PERPENDICULAR TO A NONCONDUCTING BOUNDARY



CORRECTION FACTOR FOR PROBES PARALLEL TO A NONCONDUCTING BOUNDARY

true for a conducting boundary.

(b) Measurement of Sheet Resistivity

The four-point probe was applied by Smits (18) to the problem of measuring the sheet resistivities of diffused surface layers, which may be considered to be two-dimensional. He shows that a dipole current source on an infinite sheet gives rise to the logarithmic potential

$$\phi = \frac{I \rho_s}{2 \pi} \ln \frac{r_1}{r_2} \quad (4.7)$$

where  $I$  is the current,  $\rho_s$  the sheet resistivity and  $r_1$  and  $r_2$  the distances from the point of measurement to the two sources comprising the dipole.

In this case, the dipole is made up of probes 1 and 4, so that, if we have equal probe separation, the potentials at probes 2 and 3 are given by  $\frac{I \rho_s}{2 \pi} \ln \frac{2s}{s}$   
 $= \frac{I \rho_s}{2 \pi} \ln 2$ , but are of opposite sign, so that the

potential measured is

$$V = \Delta \phi = \frac{I \rho_s}{\pi} \ln 2 \quad (4.8)$$

from which it follows that the sheet surface resistivity may be computed as

$$\rho_s = 4.53 \frac{V}{I} \quad (4.9)$$

If  $V$  is in volts and  $I$  in amp., then  $\rho_s$  is given in ohms, although sometimes ohms/square is used to indicate that it is a two-dimensional property.

If the probes are near the edge of the sample,

then image current sources are again present, and correction factors similar to those discussed above must be applied.

## 4.2 Experimental

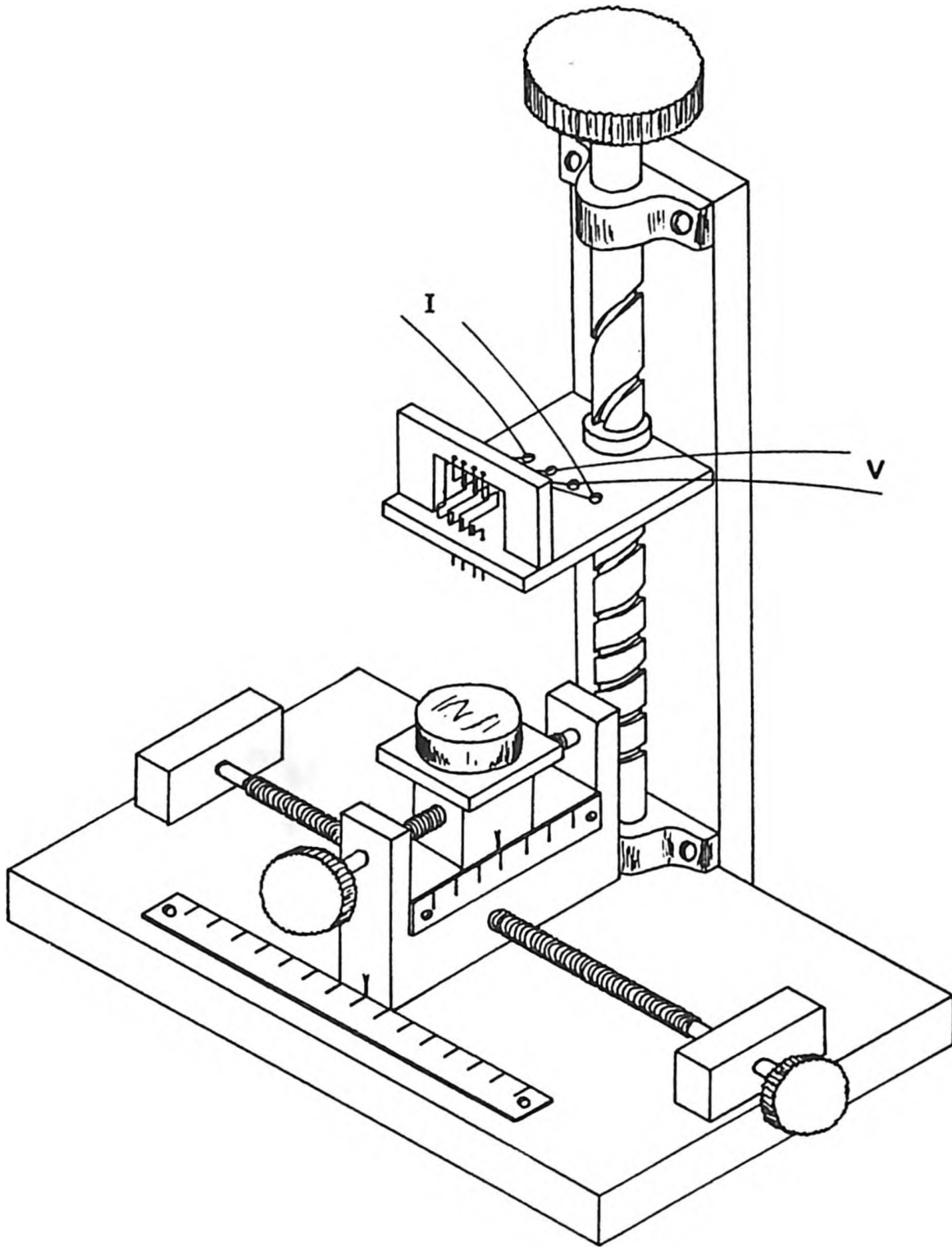
### (a) Apparatus

The apparatus used to carry out the four-point probe measurements is shown in Figure 8. The sample is placed on a micrometer table, so that the probes may be lowered on any section of the surface desired. The two scales enable the displacement of the sample to be measured to  $\frac{1}{64}$  " in either direction.

The probes themselves are .015 in. diameter tungsten wires ground to a sharp point. A probe spacing of .05 in. is achieved by passing the wires through holes of a slightly larger diameter in the horizontal support. They are then bent in an "S" shape to provide a "spring-loaded" action which ensures a good, uniform contact with the sample surface. Thin insulating sheets are placed between the "S-bends" to guard against shorting between probes. The wires then pass through horizontal holes in the upright support, also of a slightly larger diameter, so that when pressure is applied the only movement is in the "S-bend". Finally they are attached to four terminal screws, where contact is made with the current and voltage leads.

The entire probe-mount is raised and lowered by means of a vertically-mounted gear which is threaded so as to give greater sensitivity when the mount is at the lower end. The probes were pressed sufficiently firmly onto the

FIGURE 6



THE FOUR-POINT PROBE APPARATUS

surface of the sample to give stable and self-consistent readings without damaging either the probes or the sample surface. The same setting was used for all measurements during any given experiment, but the probes were raised after each measurement, to avoid the damage to the points and alteration in probe spacing which would be incurred by dragging them across the surface of the sample.

(b) Reliability Determination

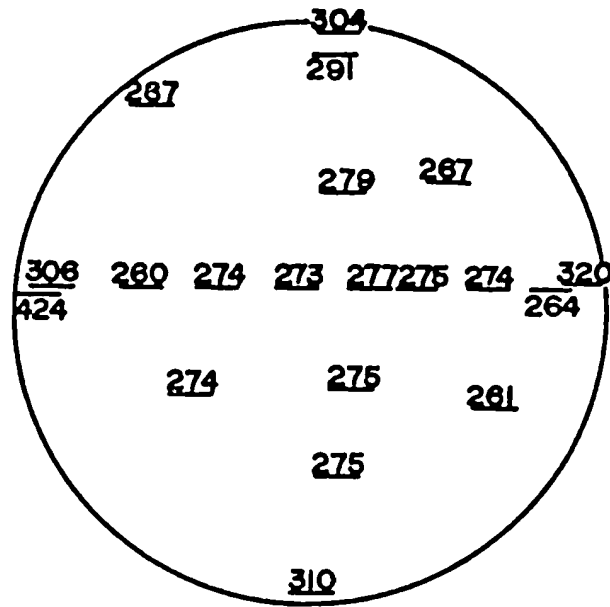
As an initial experiment to determine the reliability of the four-point probe method and apparatus, a survey was made of the surface of a slice of p-type silicon prepared for the lithium alloy. The resistivity of this material was known to be  $270 \pm 10$  ohm-cm. Figure 9 shows the results obtained in different areas of the surface by the application of eq. 4.5. The effect of the image sources on those readings taken near the edge may easily be seen. Figure 10 shows the results after the correction factor of eq. 4.6 had been applied. These results are considered to be consistent with the known value.

As a check on the validity of the surface resistivity theory, a measurement was made on the surface of a small piece of germanium. In the case of a thin sample, the resistivity is given by

$$\rho = \rho_s d G\left(\frac{d}{s}\right) \quad (4.10)$$

where  $\rho_s$  is given by eq. 4.9 (with image corrections) and  $d$  is the depth of the sample.  $G$  is another correction

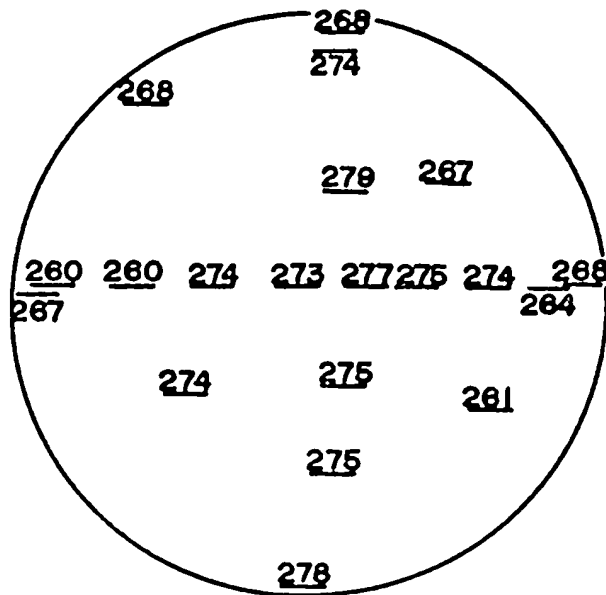
FIGURE 9



SILICON RESISTIVITY FROM EQUATION 4.5

SCALE · X 4  
 READINGS · OHM-CM  
 ERROR · ±10 OHM-CM

FIGURE 10



SILICON RESISTIVITY FROM EQUATION 4.6

factor which is determined by the method of images (19), its value approaches unity as  $d$  approaches zero.

Using eq. 4.10, the resistivity of the germanium was determined to be  $38 \pm 6$  ohm-cm. The large error is due to uncertainties in the several boundary conditions which had to be applied on account of the small size of the sample. The result is felt to be in reasonable agreement with the known value of 40 ohm-cm.

(c) Measurement of Alloy Depth and Uniformity

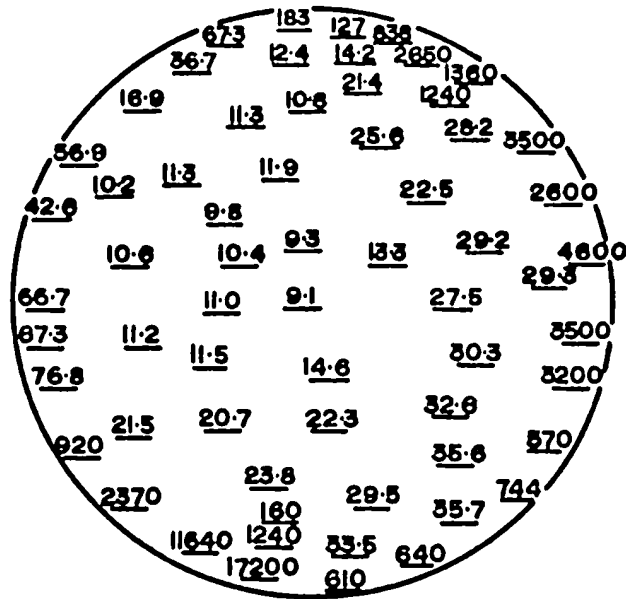
From the above preliminary measurements, the four-point probe apparatus was concluded to be functioning satisfactorily and a determination of the uniformity and depth of the lithium diffusion was undertaken. A detailed survey of an alloyed surface was carried out and the surface resistivity was calculated from eq. 4.9 with boundary corrections applied where necessary. Figure 11 shows the results of this survey.

The surface resistivity at any point ("point" here must be considered as the length covered by the probes, about 4 mm.) may be used to determine the depth of the lithium diffusion at that point in the following manner. We have from Chapter II that

$$N(x,t) = N_0 \operatorname{erfc} \left( \frac{x}{2\sqrt{Dt}} \right) \quad (2.7)$$

where in our case  $N$  is the density of the lithium atoms. At the junction depth,  $x=c$ , the concentration of lithium

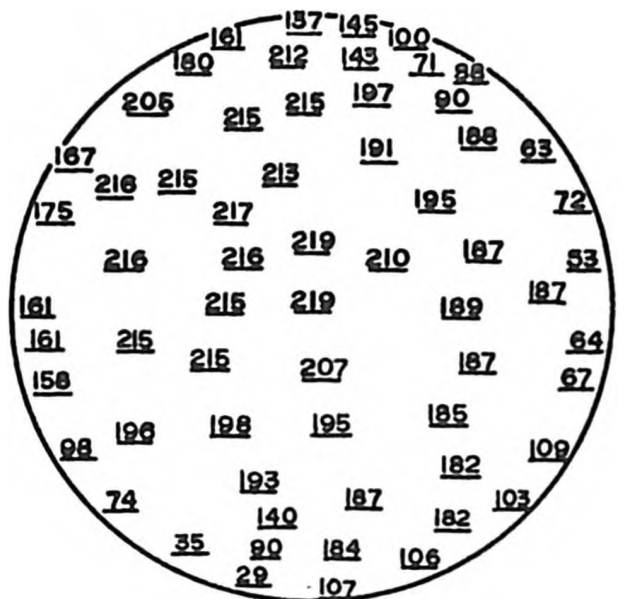
FIGURE 11



$\rho_s$  (OHMS) OF ALLOYED SURFACE

SCALE · X 4

FIGURE 12



THEORETICAL ALLOY DEPTH (MICRONS ±15)

atoms must equal the concentration of boron atoms, so that if the latter is represented by  $N_B$ , eq. 2.7 becomes

$$N_B = N_0 \operatorname{erfc}\left(\frac{c}{2\sqrt{Dt}}\right) \quad (4.11)$$

$N_B$  may be determined from the resistivity of the p-type silicon using

$$N_B = \frac{1}{\rho e \mu} \quad (4.12)$$

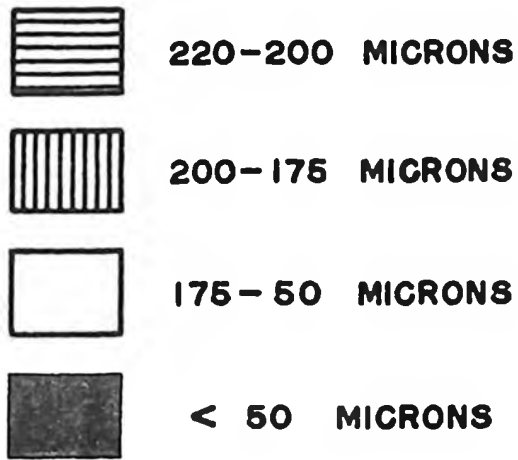
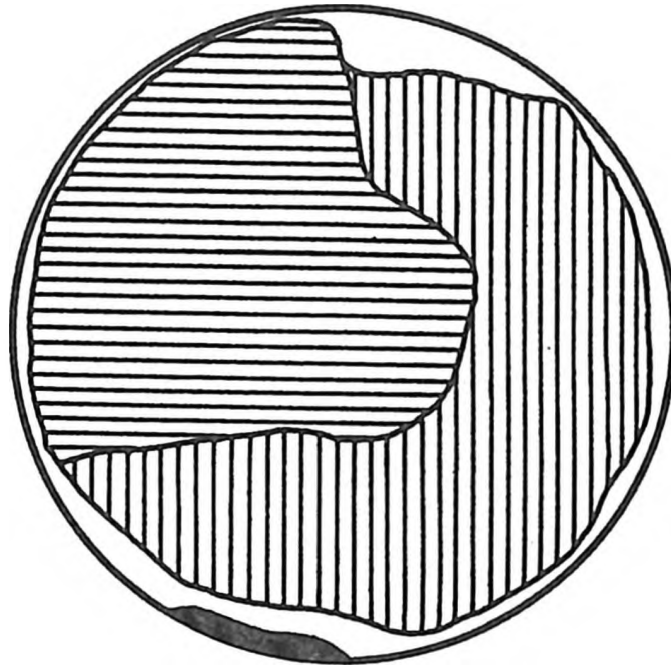
where  $N_B$  is in atoms/cm.<sup>3</sup>,  $\rho$  is in ohm-cm.,  $e$  is the electronic charge in coulombs and  $\mu$  is the hole mobility in cm.<sup>2</sup>/volt-sec., which is itself a function of the resistivity (20). Pell (21) has found that the diffusion constant  $D$  is given by

$$D = (2.5 \pm .2) \times 10^{-3} \exp\left(\frac{-6.55e}{kT}\right) \text{ cm.}^2/\text{sec} \quad (4.13)$$

Thus in eq. 4.11 there are two unknowns,  $N_0$ , the surface concentration of lithium, and  $c$ . These two quantities, however, may be related by means of graphs published by several authors (22, 23) using the measured value of the surface resistivity. The junction depth  $c$  may therefore be determined by a series of converging approximations.

Figure 12 shows the result of carrying out this procedure on all the resistivity measurements shown in Figure 11, while Figure 13 gives a topographical representation. Two features of this last figure should be mentioned. First, it is clear that much of the lithium oil has withdrawn from the edge of the silicon slice during

FIGURE 13



DEPTH CONTOUR OF ALLOYED SURFACE

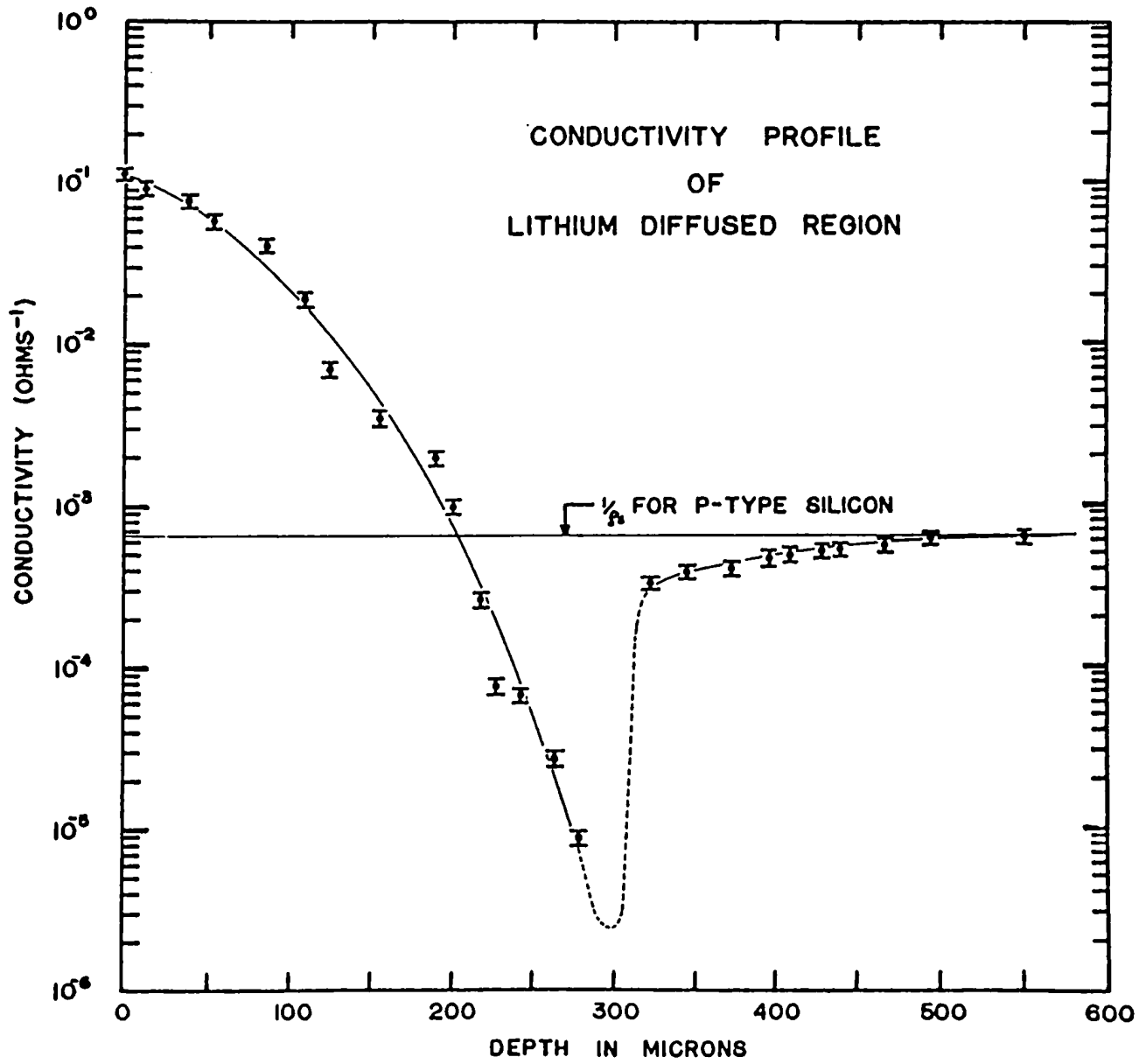
the early stages of the heating so that a considerably reduced junction depth results in this perimeter region. This area is generally from .5 to 1 mm., but may make isolated indentations of greater depth. It is felt, however, that only the darkened region showing a depth of less than 50 microns would need to be ground off to produce a satisfactory diode.

Second, it is evident that the junction depth is relatively uniform over the remainder of the slice although slightly greater in the left-hand region. It is possible that this portion of the slice was at a slightly higher temperature or that it had sustained greater surface damage. Either of these conditions would cause the lithium to diffuse more rapidly in this region.

After the survey of the surface resistivity was completed, a destructive process was carried out to determine the actual depth of the alloy. Layers approximately 25 microns thick were removed from the alloyed surface and after each lapping the surface resistivity was measured at the center of the newly-exposed face. The results are shown in Figure 14. The junction is located at the point where the resistivity reaches a maximum and therefore the conductivity a minimum. This occurs at a depth between 290 and 310 microns.

A more accurate estimate of the junction depth may be obtained by plotting the lithium concentration

FIGURE 14



as a function of depth. It may be easily seen that at any depth  $x$  above the junction

$$\left( \frac{d \rho_s^{-1}}{dx} \right)_x = N_x \mu_x e \quad (4.14)$$

where  $N_x$  and  $\mu_x$  are respectively the carrier concentration and mobility at this depth. (Mobility is a function of concentration and hence of depth). Graphs relating concentration to resistivity (21) and resistivity to mobility (20) were used to determine the correct values of  $\mu$  and  $N$  by converging approximations. In determining the derivatives, the curve of Figure 14 was considered to be linear over 25 micron regions.

Eq. 4.14 applies only in the region above the junction, so that the lithium concentration may be determined only in this region. However, below the junction eqs. 4.5 and 4.12 may be used to determine the concentration of the electrically active boron remaining and subtracting this value from the original boron concentration gives the lithium concentration.

The calculated lithium concentration is shown as the solid line in Figure 15. From this it is apparent that the junction occurs at a depth of some 300 microns, considerably greater than the 220 microns predicted by the theoretical calculations described above. It may also be seen that the concentration distribution of the lithium is not a complementary error function as is predicted by the simple theory. The difference is made clear by the inclusion



in Figure 15 of a "comparison erfc" which is a complementary error function constructed so as to intersect the experimental curve at  $x = 0$  and  $x = c$ .

There are a number of factors that may account for these differences between theory and experiment. One is the surface damage caused by the preparation of the silicon described in Sec. 3.1. In this damaged region, which may extend to a depth of as much as 40 microns, the lithium will diffuse more readily than in the undamaged region. This means that the total extent of the diffusion (which is characterized by the junction depth) and the lithium concentration near the surface will both be greater than predicted.

It is also likely that the field which is created in the immediate vicinity of the junction (see section 2.2) will cause some of the lithium atoms to drift across into the p-type region. The number of ions drifted will be small, as they have appreciable mobility only when the slice is at a temperature above about  $50^{\circ}\text{C}$ ., but will result in some decrease in the lithium concentration just above the junction.

There is also a considerable assumption made in the use of eq. 4.13 to determine the value of the diffusion constant  $D$ . Pell's studies (21) involved the diffusing of relatively small concentrations of lithium for long periods of time. To use his results for the case under study

requires the assumption that the diffusion constant is independent of diffusant concentration and diffusion time. Neither of these may be the case. Indeed, it is quite likely that the diffusion constant may be greater at high concentrations. This would also result in a junction depth greater than that predicted.

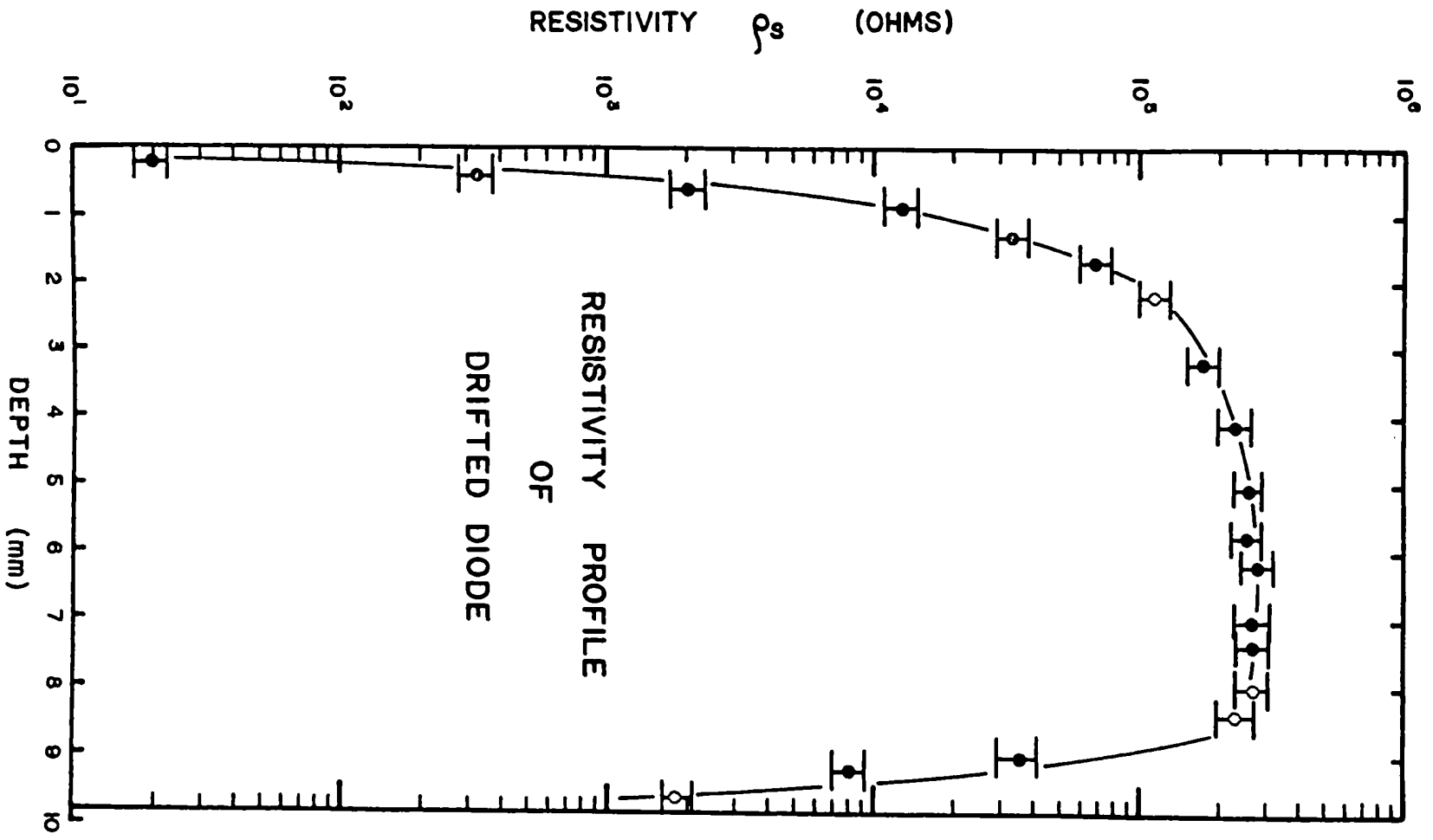
Finally, a "precipitation" or ion-pair recombination process should be mentioned. This refers to the "pairing off" of a lithium and boron atom so that the former is not "electrically active" and does not contribute to the conductivity.

For the above reasons it was concluded that four-point probe measurements do not give an accurate indication of the depth of a p-n junction. They are useful, however, for determining the uniformity of a diffusion and for comparing two diffusions carried out under similar operating conditions.

(d) Measurement of the Intrinsic Region after Drifting

The diamond saw was used to cut several cross-sectional slices from a finished detector. The surface resistivity of these slices were measured at various depths. The results were similar for each slice and a typical set is shown in Figure 16. It may be seen that the intrinsic or compensated region extends to a depth of at least 3 mm. The reason for the gradual curve of the profile near the original surface of the detector is not

FIGURE 16

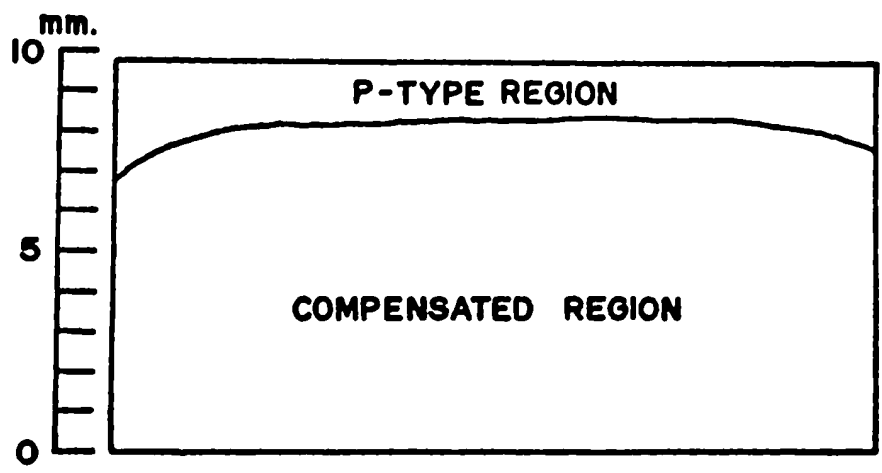


fully understood. If it is a true indication of the lithium concentration in this region, then the bias voltage applied to the detector will produce different fields in different regions and detract from the efficiency of charge collection. On the other hand, it is possible that the original p-n junction forms, in effect, a conducting boundary to the compensated region. If so, the calculated resistivity values near the surface would have to be increased considerably, as the correction factor is now greater than one. This would, of course, make a much more symmetrical graph.

The extent of the compensated region indicated by the probe was confirmed by staining the slice with Hf. The results are shown in Figure 17. The p-type region appeared a dark brown, and the compensated region a heavy blue-grey. The n-type region presumably extended only about .1 mm. and was thus too small to be shown up by the stain.

As the appearance of the entire compensated region was relatively uniform it was concluded that it was almost 8.5 mm. deep in the center of the slice, although somewhat less on the edge. This "bowing" of the compensated region occurs because the fluorocarbon removes heat from the edge of the diode so that the drifting in this region takes place more slowly. This is of importance as staining the outside edge of the detector is one of the few non-destructive

FIGURE 17



**SECTIONED AND STAINED DIODE  
AFTER DRIFTING**

---

methods of determining the extent of the compensated region.  
Clearly it will not indicate the true depth of this region.

CHAPTER V  
DETECTOR RESPONSE

5.1 Mounting the Detector

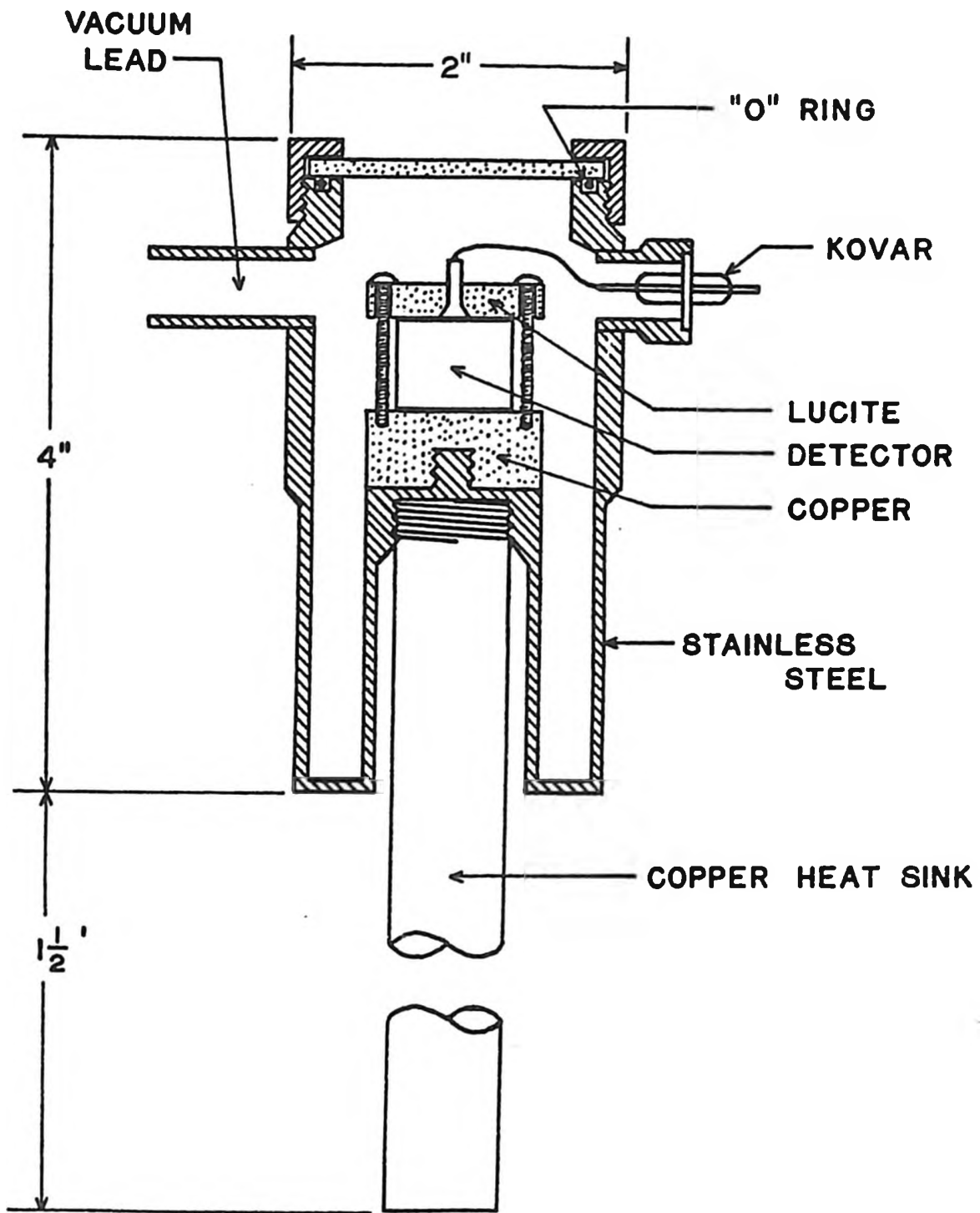
The chamber developed for mounting the completed detector is shown in cross-section in Figure 18. Electrical contact to the counter is made by means of a brass screw. Both the bias voltage and detector signal pass through a Kovar seal set in the chamber wall. A copper rod connected to the bottom of the chamber is immersed in liquid air to provide a heat sink which cools the detector in order to reduce the internal noise.

The chamber was evacuated to a pressure of  $10^{-6}$  mm., and the vacuum lead was then sealed off. Sources were placed at the side of the chamber to simplify the arrangement of the apparatus required for the coincidence experiments.

5.2 Experimental Results

In all the experiments carried out, the pulses from the detector were passed through an ORTEC #201 charge-sensitive, low-noise preamplifier and a #101 low-noise amplifier with post-amplifier. They were then sorted in a

FIGURE 18



DETECTOR CHAMBER CROSS SECTION

512-channel multichannel analyzer (MCA).

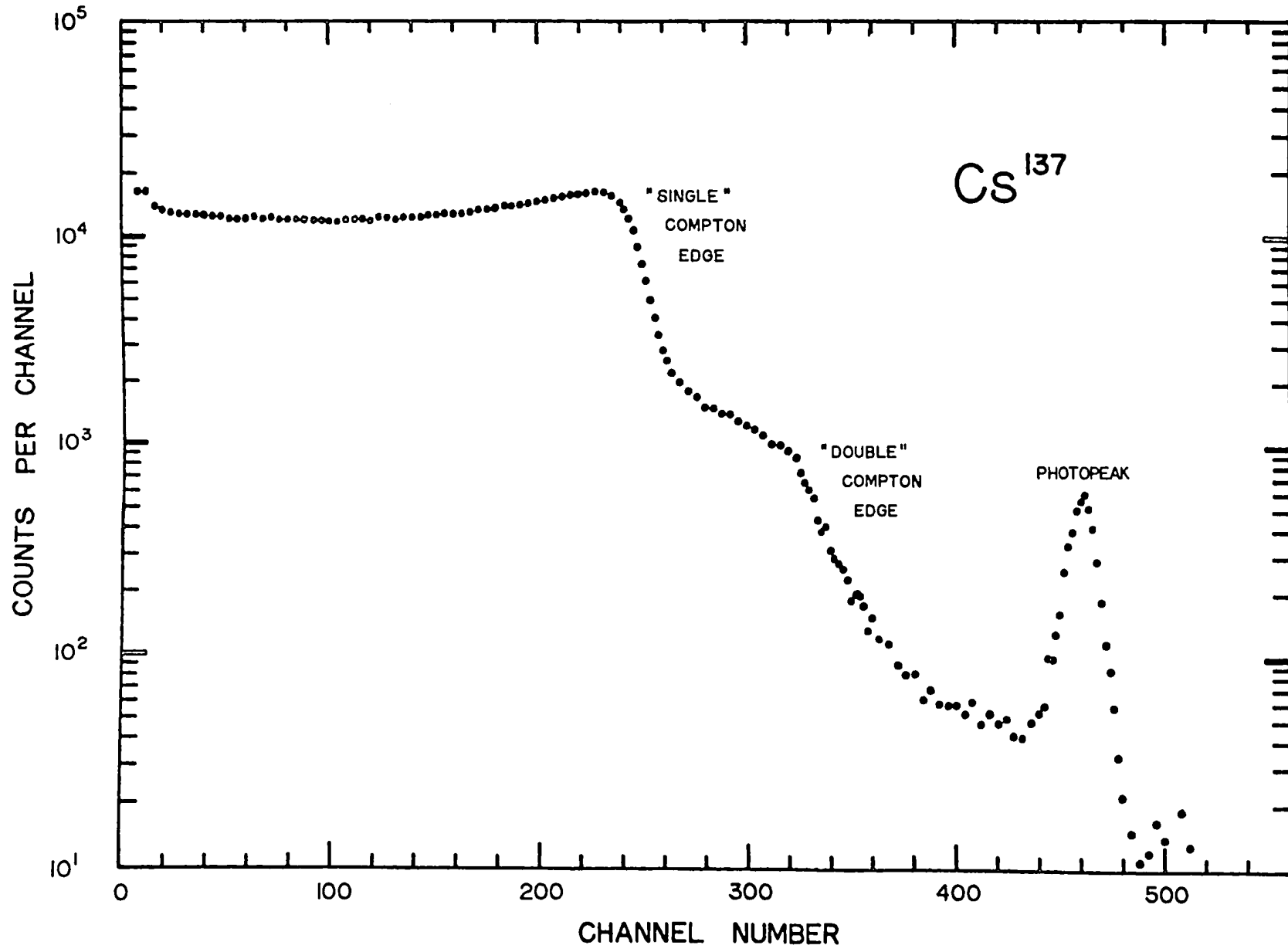
(a) Singles Spectra

The spectrum of a Cs<sup>137</sup> source is shown in Figure 19. It is immediately clear that the Compton interaction process of energy transfer to an electron dominates considerably over the photoelectric effect. This is in marked contrast to the sodium iodide counter where the total energy peak dominates the spectrum. The setting-up of a Compton spectrometer to simplify the appearance of the spectrum is described in the section following.

Also of interest is the appearance of two distinct "Compton edges" in the spectrum. The first or "single" edge corresponds to the energy given to an electron by a gamma ray which is back-scattered out of the counter. It occurs at an energy of 478 keV., so that the gamma ray retains 184 keV. If it were back-scattered again before leaving the counter it would transfer 71 keV. to this "second" Compton electron. "Collection" of both these electrons in the same pulse would lead to another Compton edge at 549 keV. This is the location of the "double" Compton edge of Figure 19.

This phenomena is of special importance in the "differential analysis" which is sometimes undertaken of complex spectra. In this analysis, the derivative of the

FIGURE 19



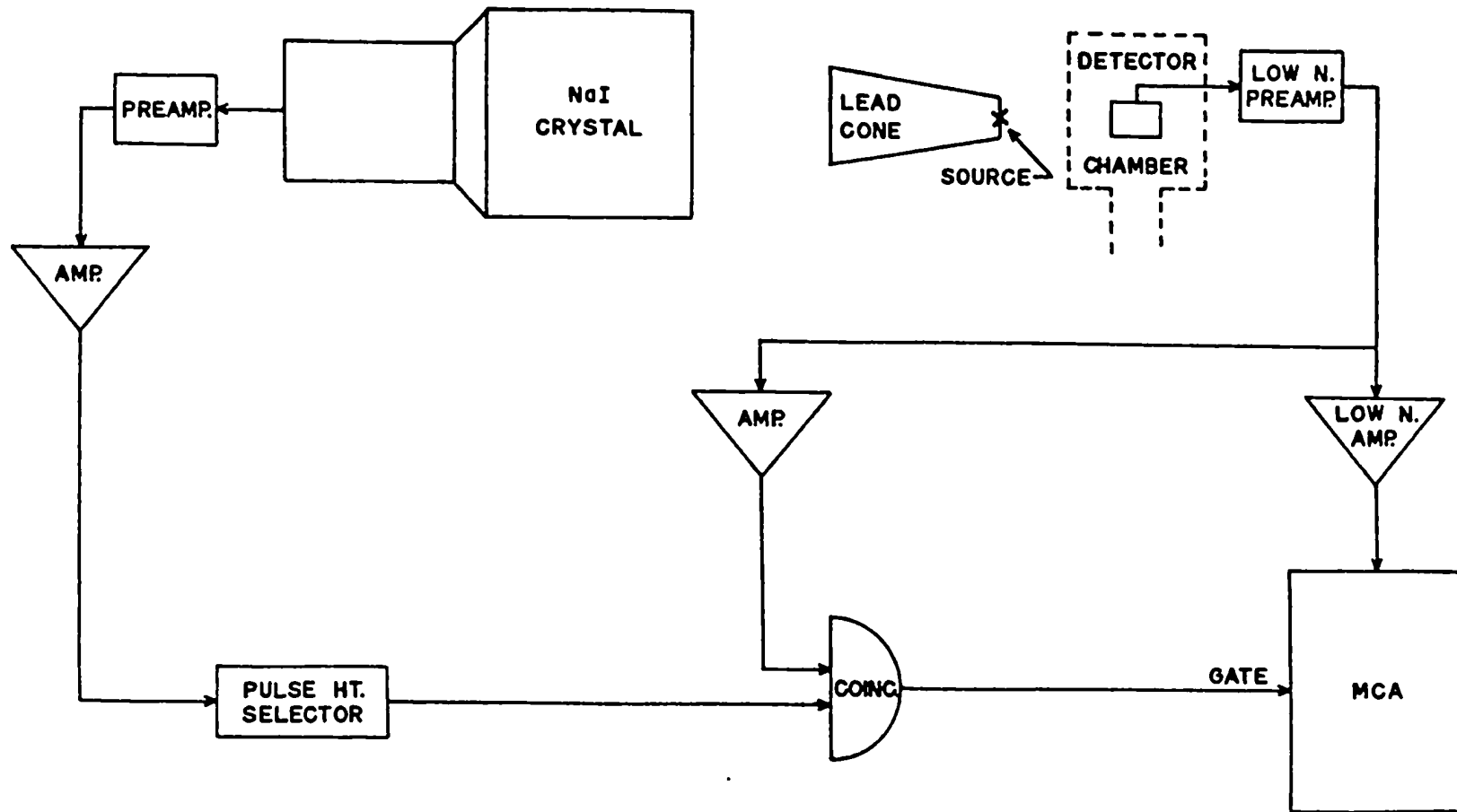
singles spectrum is calculated at closely spaced points. In the resultant differential spectrum, both the Compton edge and the photopeak will appear as distinct peaks. The presence of an additional Compton edge means that each gamma ray will now produce three peaks in the "differential spectrum", a fact which must be taken into account if a correct analysis of the spectrum is to be carried out.

(b) Compton Spectrometer

Figure 20 shows the counter arrangement used in setting up the Compton spectrometer mentioned above. The lead cone is designed to prevent gamma rays emitted by the source from being directly detected by the sodium iodide counter and perhaps giving rise to a chance coincidence with a gamma ray entering the solid state counter. Its presence reduced the chance-to-true ratio to some 10% of its former value of .1. There was also, of course, some reduction in the count rate as a greater portion of the sodium iodide counter is effectively masked from Compton scattered gamma rays as well.

The plug also acts as an effective window on the scattered gamma rays, since only those scattered out of the solid state counter at an angle of between about  $150^\circ$  and  $170^\circ$  can enter the crystal. This means, of course, that their energy range will also be limited. A pulse height selector is included to ensure that all pulses in this part of the coincidence circuit do indeed correspond to back-scattered

FIGURE 20



COMPTON SPECTROMETER SYSTEM

gamma rays.

The response of the spectrometer to various standard sources is shown in Figure 21. The response function is characterized by a single peak which is somewhat skewed in appearance and a uniform tail which extends back to zero energy. This tail is probably caused by Compton electrons being scattered so as to pass out of the sensitive region of the counter before being stopped, so that only a portion of their energy is used to create hole-electron pairs. The tail-to-peak height ratio is almost a constant, so that the tail-to-peak area ratio increases with energy. This is to be expected, since a higher energy electron will have a greater penetration depth in the counter and thus will have a greater probability of escaping from the sensitive region.

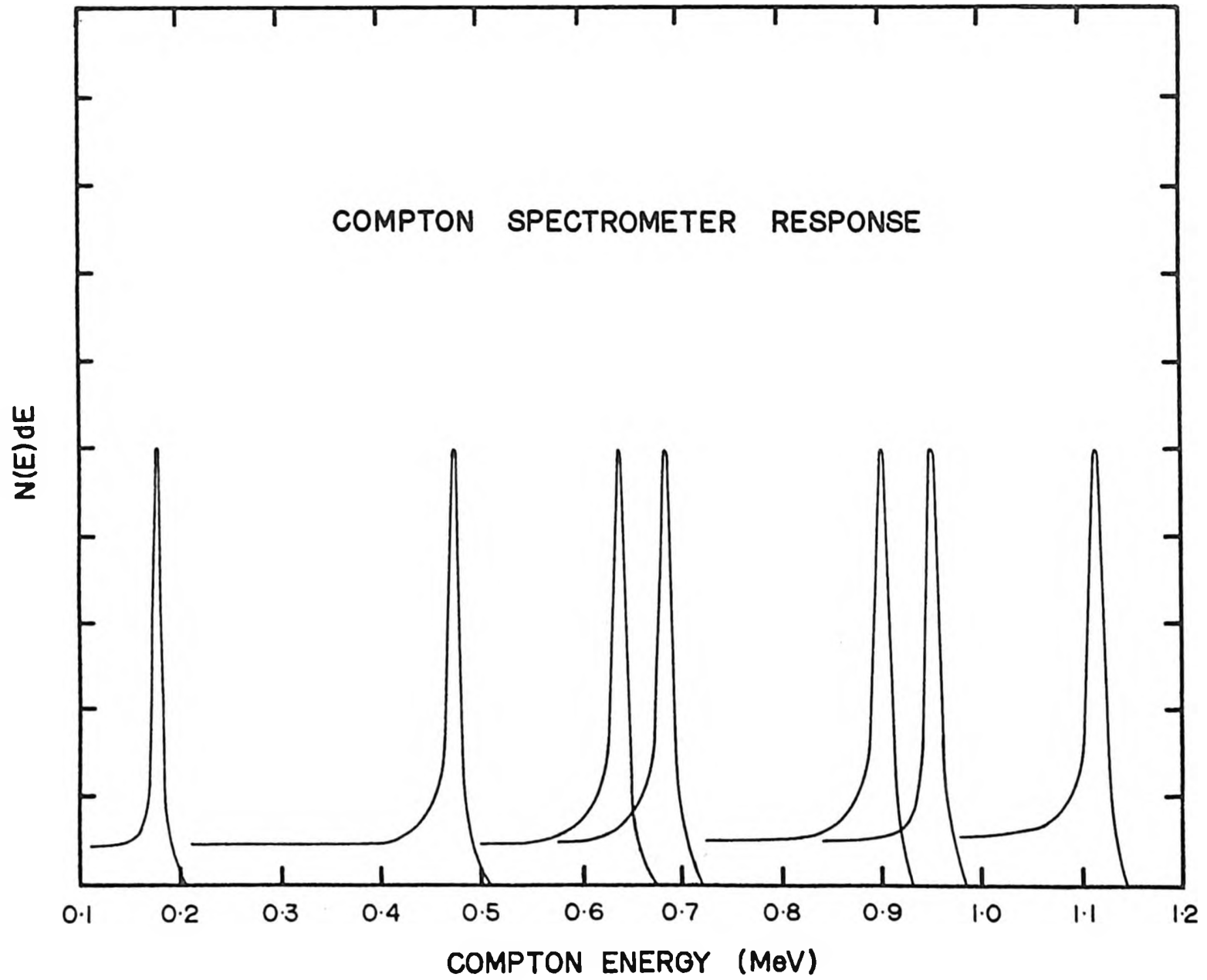
It would seem reasonable that the standard deviation of the Compton peak,  $\sigma$ , may be given by

$$\sigma^2 = \delta^2 + \eta^2 + \Delta^2 \quad (5.1)$$

where  $\delta$  is the contribution to the deviation due to the noise fluctuations in the counter and electronics,  $\eta$  is the contribution to the deviation by the statistical fluctuations in the number of hole-electron pairs (see sec. 2.5) and  $\Delta$  is the deviation introduced by the finite aperture of the NaI counter.

The experimental values for the deviations in the various peaks of Figure 21 were calculated from

FIGURE 21



$$\sigma^2 = \frac{\sum_n (\bar{n} - n)^2 N(n)}{\sum_n N(n)} \quad (5.2)$$

where  $n$  is an index for the channels occupied by the peak, and  $\bar{n}$  is the "average" channel of the peak, i.e.,

$$\bar{n} = \frac{\sum_n N(n) \cdot n}{\sum_n N(n)} \quad (5.3)$$

Due to the skewness of the peaks,  $\bar{n}$  was generally some two channels below that containing the most counts.

A set of "calculated" values for these  $\sigma$ 's was calculated from eq. 5.1. The value of  $\delta^2$  was computed by applying eq. 5.2 to the photopeak of Figure 19 and subtracting from the resultant  $\sigma^2$  the value of  $\mu^2$  for that energy. The value of  $\delta^2$  obtained was 23.96 keV.<sup>2</sup>

$\Delta^2$  may be determined from a consideration of the Compton interaction equation

$$E_{ce} = \frac{E_\gamma^2}{M_e c^2} \cdot \cos \theta \quad (5.4)$$

$$E_{ce} = \frac{1 + \frac{E_\gamma}{M_e c^2} (1 - \cos \theta)}{1 + \frac{E_\gamma}{M_e c^2} (1 - \cos \theta)}$$

where  $E_{ce}$  and  $E_\gamma$  are the Compton electron and incoming gamma ray energies respectively,  $M_e c^2$  is the electron rest energy and  $\theta$  is angle through which the gamma ray is scattered.

For a small energy change we may write  $\frac{\Delta E_{ce}}{\Delta \theta} = \frac{dE_{ce}}{d\theta}$ ,

whence

$$\Delta = \left( \frac{\frac{E_{\gamma}}{M_0 c^2} \cdot \sin \Theta}{\left[ \frac{1+E_{\gamma}}{M_0 c^2} (1-\cos \Theta) \right]^2} \right) \Delta \Theta \quad (5.5)$$

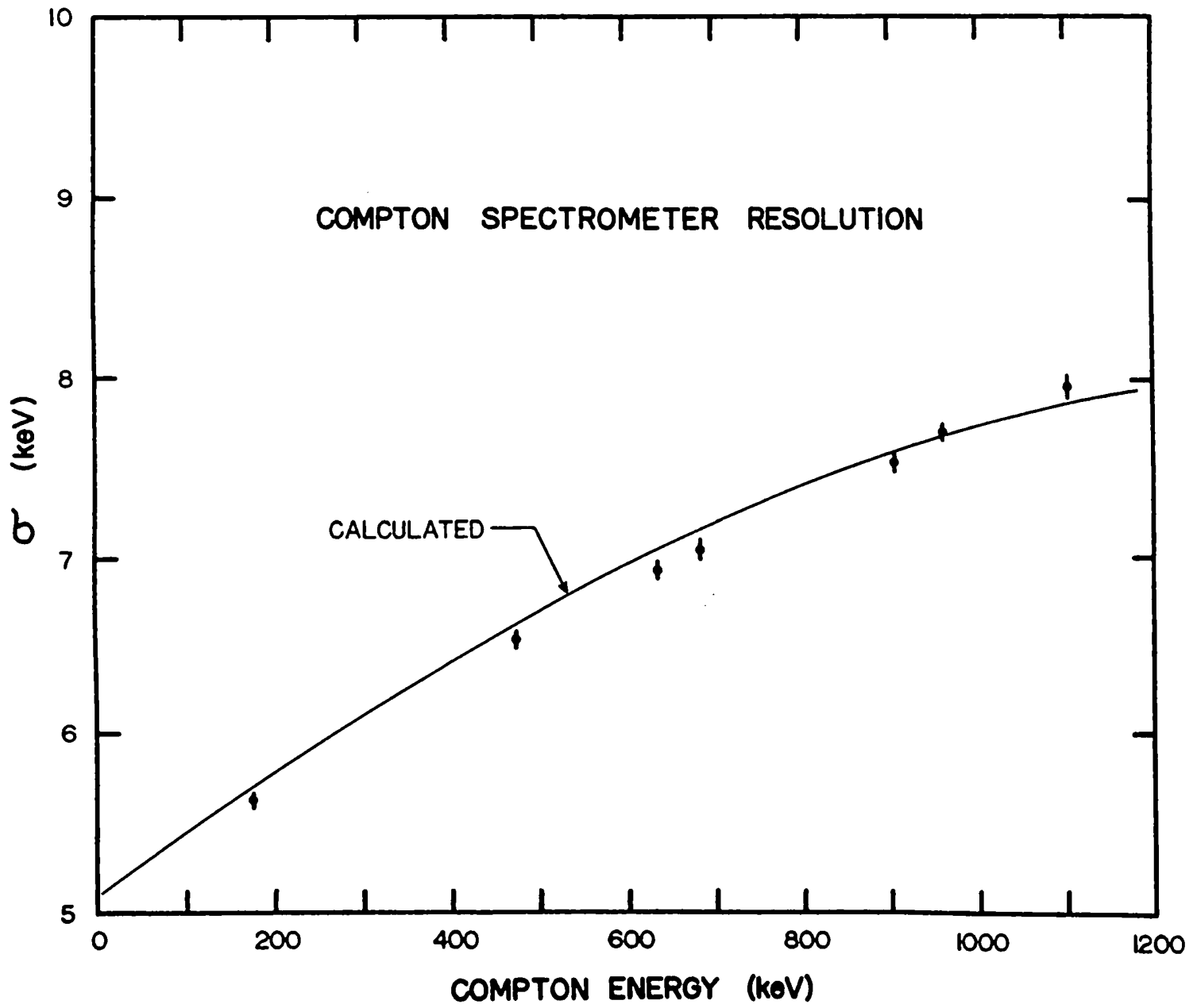
The value of  $\Theta$ , the mean angle through which the gamma rays are scattered, was considered to be  $160^\circ$  (a weak dependence of  $\sigma$  upon  $\Theta$  meant that a geometrical estimate was sufficient). However, an accurate estimate of  $\Delta \Theta$  could not be obtained from the geometry because the angular response of the crystal was not known. Instead, an average of the values of  $\Delta \Theta$  required to give agreement between the calculated and experimental values of  $\sigma$  for three highest energies was used.

Figure 22 shows the results of these calculations. The error in  $\sigma^2$  is given by

$$\Delta(\sigma^2) = \sum_n \left( \frac{\partial \sigma^2}{\partial n} \right) \cdot N(n) \quad (5.6)$$

as there is no covariance between the points. This error was generally about 2% so that the error in the experimental points is some 1%.

The value of  $\Delta \Theta$  calculated from the fitting described above was  $10.4^\circ$ , which is somewhat below the  $13^\circ$  estimated from the geometry of the system. This is consistent as it is known that a complete response is not obtained at the outer edge of the sodium iodide crystal. It is moreover probable that this response, and hence the value of  $\Delta \Theta$ ,



changes with energy, which may account for the low energy experimental points being consistently below the calculated curve.

The dependence of the counter resolution upon two operating parameters, window width and sodium iodide counter position, was also investigated. The results are shown in Tables I and II. The FWHM (peak width at half the peak maximum) has been used rather than the standard deviation because it is more easily calculated and in this case only relative values are required. The two widths are related by

$$\text{FWHM} = 2.35 \sigma \quad (5.7)$$

It may be seen that there is only a slight variation of resolution with window width. This is because most of the window is provided by the lead plug whose effect, of course, remains the same. A considerably stronger variation is observed when the distance  $x$  between the sodium iodide counter and the lead plug is varied. Increasing the distance  $x$  decreases the angular spread  $\Delta\theta$  of the gamma rays entering the crystal which in turn results in a direct decrease in the component of the overall resolution. The resolution improvement is, of course, accompanied by a decrease in the count rate, so that the position of the crystal for any given experiment must be determined by a consideration of both the statistics and resolution required for useful results.

TABLE I

Compton Spectrometer Response and Window Width

Window Width (Full Width = 10)	FWHM (keV.) $\pm .5$	Count Rate (Counts/Min)
2.3	13.0	163
3.0	13.2	165
4.0	13.5	169
4.5	13.4	172
5.2	13.7	177
10.0	14.2	180

TABLE II

Compton Spectrometer Response and NaI Crystal Position

x = distance from plug to NaI crystal

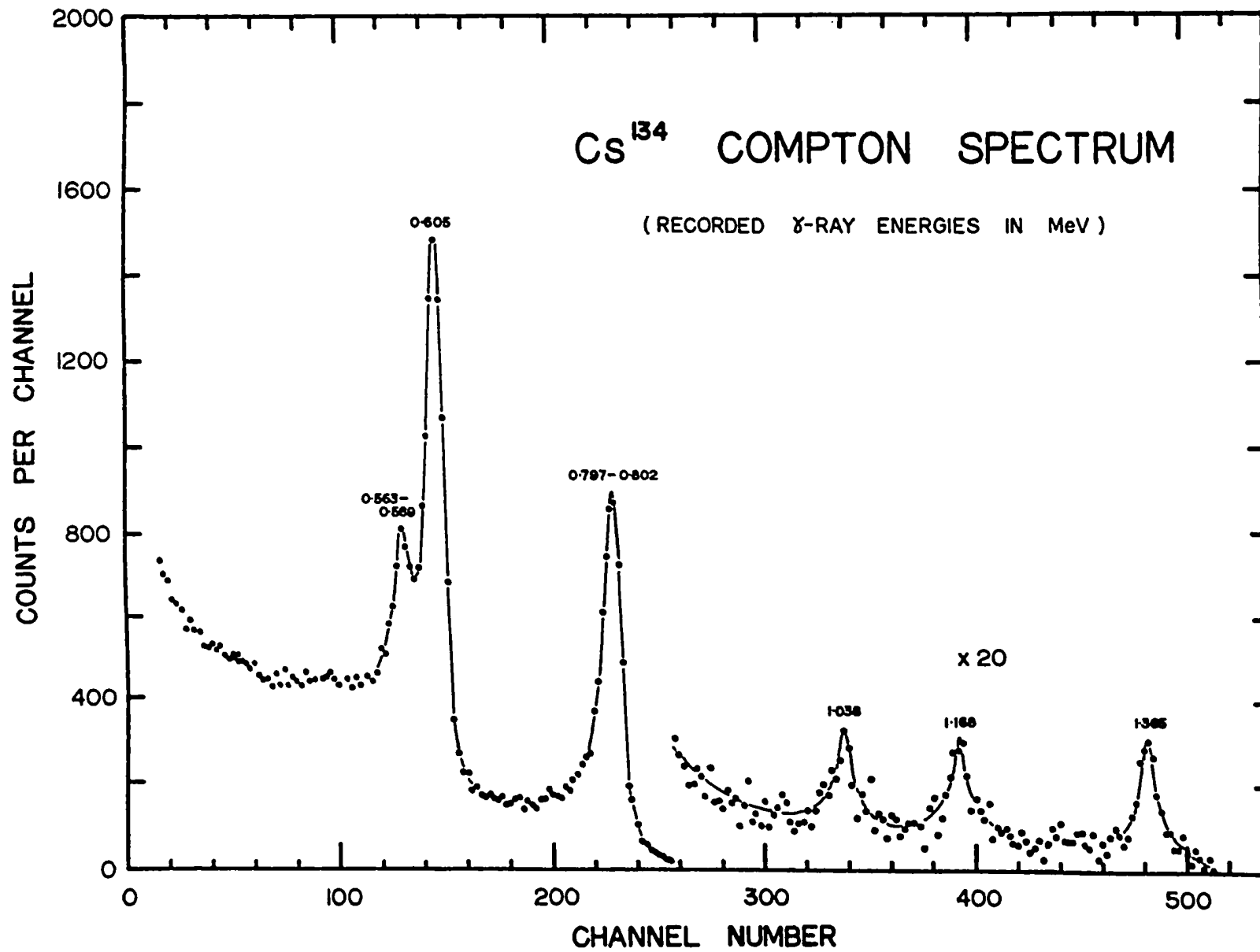
x (cm.)	FWHM (keV.) $\pm .5$	Count Rate (Counts/Min)
0	16.4	305
2.0	14.7	218
3.5	13.1	156
5.5	12.5	107

(c) Spectrum of Cs<sup>134</sup>

The spectrum of Cs<sup>134</sup> taken with the Compton spectrometer is presented in Figure 23 to illustrate the considerable improvement in gamma ray spectroscopy which may be expected from the development of lithium-drifted detectors. The 563-569 keV. doublet is clearly resolved from the 605 peak, a separation which could not be achieved with a sodium iodide counter as the resolution of these counters is at best some 7%, while a 3% resolution is necessary in this case. The result could be obtained with a Siegbahn magnetic spectrometer, but the process would be a much slower one as only a small section of the spectrum may be taken at any one time.

The 565 and 800 keV. peaks, whose components are not at all resolved as they are only some 5 keV. apart, may at least be immediately identified as doublet peaks, as their widths are 16 and 20 keV. respectively, in comparison to the 14 and 17 keV. widths predicted by Figure 22. The two component energies could be easily determined by the use of a coincidence spectrometer.

A spectrum of true gamma ray energies may be obtained by using the solid state counter in a pair spectrometer system. The 2.490 and 2.506 MeV. peaks of Ga<sup>72</sup> have been clearly resolved using a system of this type. This corresponds to a resolution of less than 1%.



The development of lithium-drifted detectors must therefore be considered as a major contribution to high resolution gamma ray spectroscopy, particularly in the field of short-lived isotopes.

## REFERENCES

1. K. G. McKay, Phys. Rev. 76, 1537 (1949)
2. K. G. McKay, Phys. Rev. 84, 829 (1951)
3. S. S. Friedland, J. W. Mayer, J. M. Denney and F. Keywell, Rev. Sci. Instr. 31, 74 (1960)
4. J. L. Blankenship and C. J. Borkowski, I.R.E. Trans. Nuc. Sci. NS8, 17 (1961)
5. E. H. Pell, J. Appl. Phys. 31, 291 (1960)
6. J. H. Elliot, Nucl. Instr. and Meth. 12, 60 (1961)
7. J. W. Mayer, N. A. Bailey and H. L. Dunlap, Nuclear Electronics 1, 567, International Atomic Energy Agency, Vienna (1962)
8. C. A. J. Ammerlan and K. Mulder, Nucl. Instr. and Meth. 21, 97 (1963)
9. G. L. Miller, B. D. Pate and S. Wagner, I.E.E.E. Trans. Nuc. Sci. NS10, 220 (1963)
10. W. Shockley, Czech. J. Phys. B11, 81 (1961)
11. G. D. O'Kelley, Detection and Measurement of Nuclear Radiation, NAS-NS-3107, 53, Office of Tech. Services, Dept. of Commerce, Washington, D.C. (1962)
12. G. Dearnely and D. C. Northrop, Semiconductor Counters for Nuclear Radiations, 124, Spon (1963)
13. B. I. Boltaks, Diffusion in Semiconductors, 94, Academic Press (1963)
14. W. Shockley, Electrons and Holes in Semiconductors, 324, Van Nostrand (1950)
15. M. H. Sullivan and J. H. Eigler, J. Electrochem. Soc. 104, 266 (1957)
16. L. B. Valdes, Proc. I.R.E. 42, 420 (1954)
17. L. B. Valdes, Proc. I.R.E. 40, 1420 (1952)

## REFERENCES

18. F. M. Smits, Bell Sys. Tech. J. 37, 711 (1958)
19. J. Uhler, Bell Sys. Tech. J. 34, 105 (1955)
20. F. J. Morin and J. P. Maita, Phys. Rev. 96, 28 (1954)
21. E. M. Pell, Phys. Rev. 119, 1222 (1960)
22. G. Backenstoss, Bell Sys. Tech. J. 37, 699 (1958)
23. J. C. Irvin, Bell Sys. Tech. J. 41, 411 (1962)